A portable reflected-sunlight spectrometer for CO_2 and CH_4

Benedikt A. Löw[1], Ralph Kleinschek[1], Vincent Enders[1], Stanley P. Sander[4], Thomas J. Pongetti[4], Tobias D. Schmitt[1], Frank Hase[5], Julian Kostinek[6], and André Butz[1,2,3]

[1]Institute of Environmental Physics (IUP), Heidelberg University, Germany
[2]Heidelberg Center for the Environment (HCE), Heidelberg University, Germany
[3]Interdisciplinary Center for Scientific Computing (IWR), Heidelberg University, Germany
[4]Jet Propulsion Laboratory, California Institute of Technology, Pasadena, USA
[5]Karlsruhe Institute of Technology (KIT), Institute of Meteorology and Climate Research (IMK-ASF), Karlsruhe, Germany
[6]School of Engineering and Applied Sciences, Harvard University, Cambridge, MA, USA

Correspondence: Benedikt Löw (benedikt.loew@iup.uni-heidelberg.de)

Abstract. Mapping the greenhouse gases carbon dioxide (CO_2) and methane (CH_4) above source regions such as urban areas can deliver insights into the distribution and dynamics of the local emission patterns. Here, we present the prototype development and an initial performance evaluation of a portable spectrometer that allows for measuring CO_2 and CH_4 concentrations integrated along a long ($> 10\,\mathrm{km}$) horizontal path component through the atmospheric boundary layer above a target region. To this end, the spectrometer is positioned at an elevated site from which it points downward at reflection targets in the region collecting the reflected sunlight at shallow viewing angles. The path-integrated CO_2 and CH_4 concentrations are inferred from the absorption fingerprint in the shortwave-infrared (SWIR) spectral range. While mimicking the concept of the stationary CLARS-FTS (California Laboratory for Atmospheric Remote Sensing - Fourier Transform Spectrometer) at Los Angeles, our portable setup requires minimal infrastructures and is straightforward to duplicate and to operate at various places.

For performance evaluation, we deployed the instrument, termed EM27/SCA, side-by-side with the CLARS-FTS at Mt. Wilson observatory (1670 m a.s.l.) above Los Angeles for a month-long period in Apr./May 2022. We determined the relative precision of the retrieved slant column densities (SCDs) for urban reflection targets to 0.36–0.55% for O_2, CO_2 and CH_4, where O_2 is relevant for lightpath estimation. For the partial vertical column (VCD) below instrument level, which is the quantity carrying the emission information, the propagated precision errors amount to 0.75–2% for the three gases depending on the distance to the reflection target and solar zenith angle. The comparison to simultaneous CLARS-FTS measurements shows good consistency, but the observed diurnal patterns highlight the need for taking into account light scattering to enable detection of emission patterns.

1 Introduction

Cities are hotspots for emissions of the greenhouse gases carbon dioxide (CO_2) and methane (CH_4) (e.g. Edenhofer et al., 2014; Gurney et al., 2021; Mitchell et al., 2022; de Foy et al., 2023). The major sources are traffic and heating related emissions, fossil fuel based electricity production, natural gas leakages, and waste treatment (e.g. Gurney et al., 2019; Sargent et al., 2021; Maasakkers et al., 2022; Huo et al., 2022). At the same time, cities have become a driving force behind climate change

mitigation plans and they have committed to ambitious reductions of their greenhouse gas emissions (e.g. Hsu et al., 2019; Wei et al., 2021; Mueller et al., 2021).

25 To support the evaluation and verification of these emission reduction plans, urban greenhouse gas measurement networks emerge (e.g. Duren and Miller, 2012; McKain et al., 2015; Turnbull et al., 2019; Turner et al., 2020; Dietrich et al., 2021), measurement campaigns (e.g. Hase et al., 2015; Pitt et al., 2022) aim at demonstrating techniques (e.g. Christen, 2014) for emission monitoring, and satellite sensors have been shown to be able to detect CO_2 domes (e.g. Reuter et al., 2019; Ye et al., 2020; Kiel et al., 2021) and localized CH_4 leakages (e.g. Maasakkers et al., 2022; de Foy et al., 2023). While the remote sensing

30 tools operated from satellites or ground typically report the column-averaged dry-air mole fractions of CO_2 (XCO_2) and CH_4 (XCH_4), in-situ measurements deliver the local concentrations. The former suffer from limited sensitivity to signals confined to the lowermost atmospheric layers and thus require superb precision to detect minute variations. The latter are prone to be affected by local variations implying limited representativeness on the scale of neighborhoods and city districts. Techniques that average the greenhouse gas concentrations along horizontal paths above cities have been suggested as a tool to bridge

35 the sensitivity gap between in-situ and column-averaged data (e.g. Fu et al., 2014; Rieker et al., 2014; Queißer et al., 2016; Griffith et al., 2018). The horizontally integrated concentrations promise better sensitivity to surface emissions than column-averaged data. Concurrently, they are more representative on kilometer-scales than urban in-situ data since they average over local emission and turbulence patterns.

The California Laboratory for Atmospheric Remote Sensing (CLARS) - Fourier Transform Spectrometer (FTS), stationed

40 on Mt. Wilson in the North of the Los Angeles (LA) basin at roughly $1700\,m$ elevation, is an observing system that delivers CO_2 and CH_4 concentrations integrated along horizontal pathlengths of a few ten kilometers (Fu et al., 2014). The CLARS-FTS points into the LA basin collecting sunlight reflected off the ground from various locations (termed *reflected-sun* configuration in the following). After reflection, the light propagates at a shallow angle quasi-horizontally through the urban boundary layer towards the observer at Mt. Wilson. From each of the collected absorption spectra, the spectral analysis provides path-integrated

45 CO_2 and CH_4 concentrations. Pointing sequentially at various reflection locations throughout the LA basin enables horizontal mapping of the urban dome of CO_2 and CH_4 with a resolution on the district scale in a few hours. Since the technique uses sunlight, its operation is limited to daytime and fair weather conditions. The spectral analysis methods need to take into account that there is a quasi-vertical lightpath component from the sun to the reflection point on the ground in addition to the quasi-horizontal component above the city, and that light scattering by particles in the atmosphere complicates the radiative

50 transfer considerations (Zhang et al., 2015; Zeng et al., 2017, 2020b). Despite these challenges, the CLARS-FTS has been delivering various insights into the spatiotemporal distribution of CO_2 and CH_4 (and carbon monoxide (CO), nitrous oxide (N_2O), water vapor isotopologues) above the LA basin and the related greenhouse gas emission patterns on the ground (Wong et al., 2015, 2016; He et al., 2019; Zeng et al., 2020a, 2021, 2023; Addington et al., 2021)

Here, we present the prototype deployment of a greenhouse gas spectrometer that mimics the observational configuration

55 of the CLARS-FTS but, unlike the latter, the proposed instrument is portable. Requiring minimal infrastructure, it can be deployed at any location with a vantage point that is elevated above a localized source region and allows for a clear view into the area. The envisaged use-cases are the replication of the CLARS-FTS experiment in places other than LA and the combined

Figure 1. The EM27/SCA instrument on top of Mt. Wilson overlooking the Los Angeles Basin. The pointing mirrors are located inside the upper metal protective housing, shielding them from direct sun light. The depicted viewing direction points away from the observer into the basin. The Lambertian reflector plate is mounted on top of the instrument's main body. The context camera is attached on the right.

deployment of several of these instruments, which would allow for crossed-beam configurations to enhance the horizontal mapping capabilities in a primitive tomographic setup. The instrument, called EM27/SCA, is a derivative of the EM27/SUN FTS, which is in operational use within the COCCON (Collaborative Carbon Column Observing Network) for measuring column-averaged gas concentrations in direct-sun configuration (Frey et al., 2019).

Our study is organized as follows. Section 2 outlines the technical developments and calibration procedures required to make the EM27/SCA work in reflected-sun configuration, while Sect. 3 reports on the conditions of co-deployment with the CLARS-FTS in LA. In Sect. 4, we summarize the spectral retrieval of the target gases CO_2, CH_4, CO and, for lightpath information, O_2 (molecular oxygen). Section 5 discusses the performance of the EM27/SCA and compares it to the simultaneous CLARS-FTS measurements. Section 6 concludes the study with an outlook on future steps.

2 Instrumentation - EM27/SCA

The EM27/SUN FTS (Gisi et al., 2012), commercially available from Bruker Optics, forms the basis of our setup. This compact and portable instrument has proven to reliably measure XCO_2 and XCH_4 in several field campaigns (e.g. Hase et al., 2015; Butz et al., 2017; Luther et al., 2019, 2022) and is the backbone instrument of the COCCON network (Frey et al., 2019). The FTS has a maximum optical path difference of $\Delta = 1.8\,\mathrm{cm}$, corresponding to a resolution of $1/\Delta = 0.56\,\mathrm{cm}^{-1}$. As the
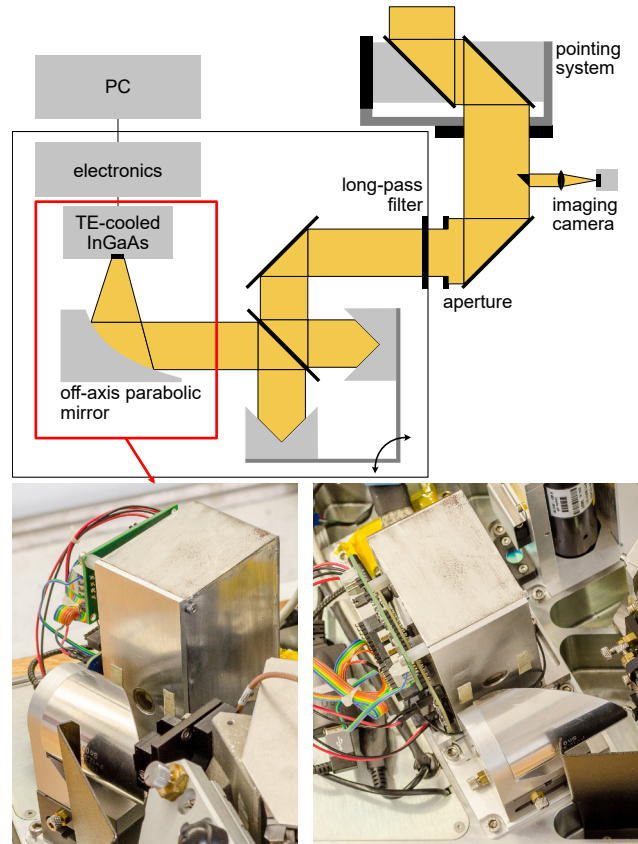
3

Figure 2. Schematics of the lightpath through the EM27/SCA (top panel). Main modifications are the custom detector module (lower panel photographs) and the imaging camera recording the FOV. Adapted from Gisi et al. (2012).

EM27/SUN is designed for direct sunlight observations, we modified several of its components to make it suitable for the fainter radiances expected when measuring sunlight reflected off the ground. Fig. 1 and 2, respectively, show a photograph of the instrument during deployment at LA, and a schematic of the modified spectrometer. We replaced the standard room-temperature detector module by a 2000 times more sensitive extended InGaAs detector (Hamamatsu G12183-203K) featuring custom-built electronics with a two-stage thermo-electric (TE) cooler set to operating temperatures of -20°C. The spectral cut-off of the detector and a foil filter mounted in front of it limit the sensitive range to 4000–12000 cm^{-1}. The 90° off-axis focusing mirror was replaced by one with 44 mm diameter and an effective focal length of $f_{\mathrm{eff}} = 33\,\mathrm{mm}$. Given a diameter of 0.3 mm of the photosensitive area of the detector diode, the full field-of-view (FOV) is 9.1 mrad (0.52°). We removed all apertures inside the instrument and mounted an adjustable iris aperture in front of the entrance window. We typically use a beam diameter of 2.6 cm. Together with the fast focusing mirror, this enhances the throughput by a factor of 70. Thus, the more sensitive detector and the increased throughput enhance the sensitivity of the EM27/SCA by a factor $\sim 10^5$ compared to the standard EM27/SUN.
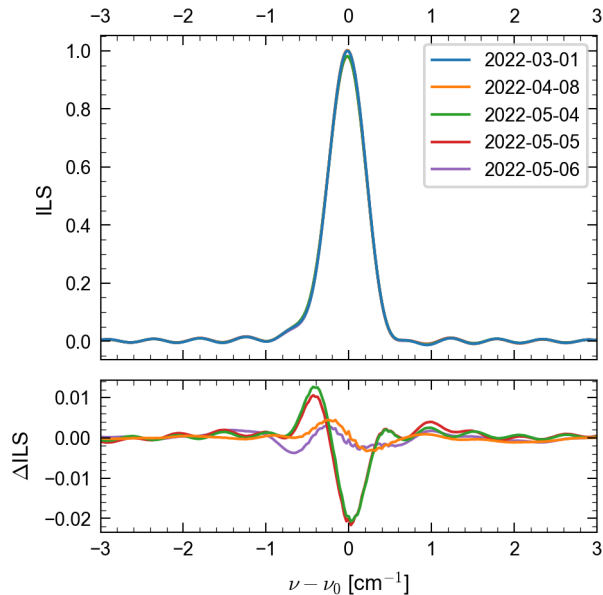
Figure 3. ILS measurements before and during the field campaign at Mt. Wilson. The ILS are normalized to unity area and subsequently scaled such that the ILS measured on Mar. 1, 2022 has a peak height of 1. The lower panel shows differences to the ILS measured on Mar. 1, 2022. The differences between measurements are within the expected repeatability.

In front of the spectrometer, the pointing system (derived from EM27/SUN's "sun-tracker") collects sunlight reflected from the ground target into the spectrometer. The pointing system is an alt-azimuthal mount consisting of two rotational stages moving two 50 mm elliptic flat mirrors in azimuthal and zenith direction. Behind the pointing mirrors, a prism couples a small portion of the parallel beam into an imaging camera boresighted with the instrument, allowing for real-time tracking of the instrument's FOV. The FOV-camera is a 1/2" CMOS sensor (1280×1024 px) with a 900 nm longpass filter and an objective lens with a focal length of $f = 100\,\text{mm}$, representing the instruments FOV with a diameter of 181 px. In addition, an identical context camera with a 185° FOV fisheye lens was mounted on the side of the instrument (see figure 1), recording the general meteorological conditions and skylight context. Finally, we mounted a horizontally levelled Zenith Lite™Lambertian reflector plate on top of the EM27/SCA's main body such that reference observations of reflected sunlight without horizontal path component ("short-cut" observations) can be carried out at any time. The diffuse reflectivity of 50% makes the brightness of the reflector plate comparable to bright ground targets.

2.1 Instrument lineshape

We determined the instrument lineshape (ILS) of the EM27/SCA from H_2O absorption lines measured in open-path configuration. Following the procedure described in Frey et al. (2015), we averaged 30 min of spectra of a halogen lamp positioned at a distance of 3.2 m while keeping ambient pressure, temperature and humidity conditions constant. From these spectra, we
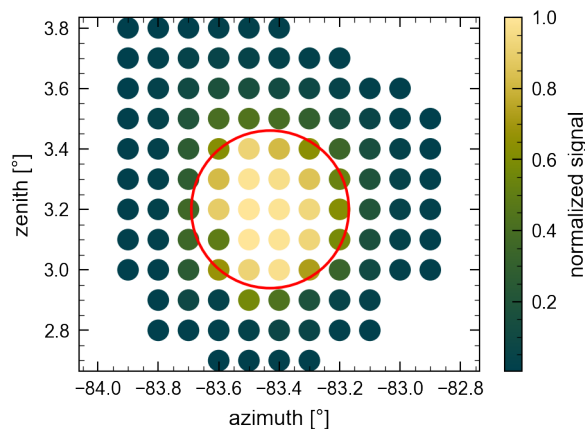
Figure 4. Mapping of the FOV of the EM27/SCA by scanning over a point source. The nominal FOV is marked in red around the estimated center.

then retrieved the ILS using the LINEFIT software (Hase et al., 1999) with Norton-Beer medium apodization. The FOV of the EM27/SCA is considerably larger than the one of the standard EM27/SUN. However, homogeneous illumination of the FOV is important for an accurate representation of the ILS. We therefore did not point the halogen lamp directly into the instrument, but instead observed the homogeneously illuminated reflector plate mounted on top of the instrument (see Fig. 1).

Figure 3 illustrates the ILS and its changes monitored during the course of the measurement campaign in LA reported below. The observed differences are within the expected repeatability of the calibration procedures in the field. The ILS has a full-width-at-half-maximum of $0.54\,\mathrm{cm}^{-1}$ and is slightly asymmetric. Due to the fast optics and larger FOV, imaging quality of the EM27/SCA is worse and optical alignment is more delicate than for the standard EM27/SUN. Limiting the beam diameter to $2.6\,\mathrm{cm}$ as described above clearly improved the width of the ILS and its symmetry.

2.2 Polarization sensitivity

FTS can exhibit sensitivity to the polarization state of the incoming light. This is mainly caused by the beamsplitter, as its reflectivity differs for light polarized parallel or orthogonal to the plane of reflection, so that the throughput differs for vertically and horizontally polarized light. We characterize the polarization sensitivity of the EM27/SCA by comparing halogen lamp spectra, which are linearly polarized in vertical or horizontal direction. In the range of $5600–8000\,\mathrm{cm}^{-1}$, the instrument is 8–10% less sensitive to horizontally than to vertically polarized light. The sensitivity difference increases towards smaller wavenumbers reaching 15% reduced sensitivity at $4500\,\mathrm{cm}^{-1}$.
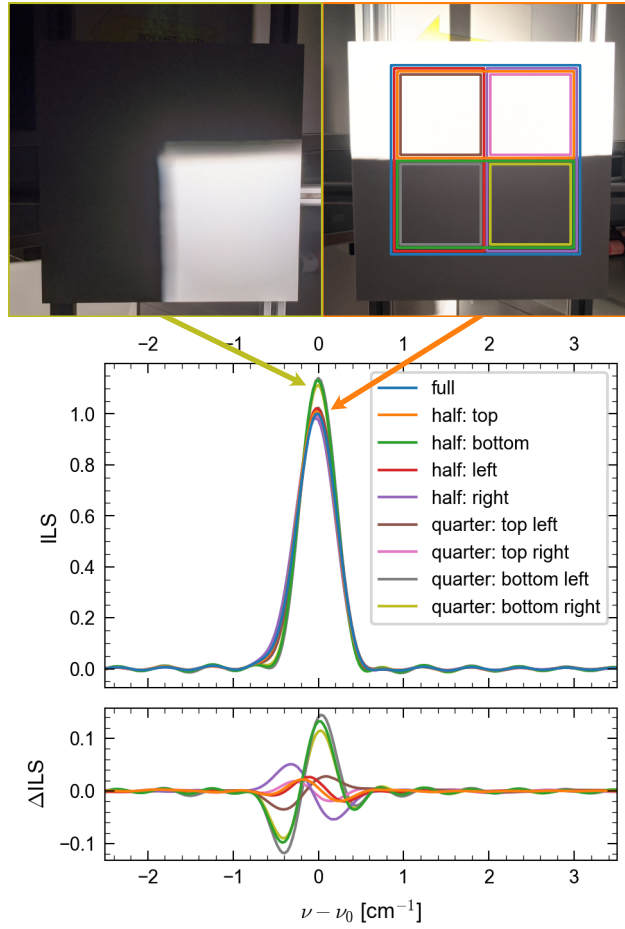
6

Figure 5. Test configuration (upper row) and ILS measurements (bottom) for an inhomogeneous illumination of the reflector plate. The variations of the ILS under different illumination patterns show that the instrument is influenced by scene inhomogeneity in extreme cases.

2.3 Field of view and scene heterogeneity

In addition to the FOV of 9.1 mrad (0.52°) calculated from the optical parameters, we empirically determined (1) the width of the FOV and (2) its position within the image of the FOV-camera. To this end, we used a collimated light source with an iris aperture.

To measure the width of the FOV, we scanned the pointing system in steps of 0.1° across the light source positioned at approximately 18 m distance from the spectrometer. Figure 4 shows the intensity mapping with the nominal FOV overlayed. The width of the measured FOV is in good agreement with the nominal FOV of 0.52° and only slightly elongated along the zenith direction. Note that the FOV rotates with changes in azimuth viewing direction. To determine the FOV position within the FOV camera image, we positioned the light source approximately 33 m away from the instrument. We determined the

pointing direction corresponding to the maximum signal. We then scanned in azimuth and zenith direction until the signal dropped by half respectively. From this, we determined the center position of the light source in the camera image as the average position of all half-maximum positions and recorded an image pointing there. We determined the center pixel of the instrument FOV inside this image from fitting an ellipse to the saturated pixels. The off-center position of the camera in the beam together with the finite distance of the light source leads to a parallax error. The camera is placed $2.5\,\mathrm{cm}$ from the beam axis. From that we estimated this error to 10% of the full FOV ($0.05°$). Additionally, we observed that the FOV drifts over the course of a day. The drift is limited to below $0.1°$, and is most likely caused by thermal expansion of the pointing system.

Real world scattering targets are only approximately homogeneous. To determine the influence of scene heterogeneity on the ILS, we set up a laboratory experiment using a $50{\times}50\,\mathrm{cm^2}$ Lambertian reflector plate located at a distance of $7\,\mathrm{m}$ from the EMS27/SCA. A halogen lamp illuminated the reflector plate homogeneously. We conducted various experiments by shading parts of the reflector plate such that only half or a quarter of the area was illuminated (Fig. 5, upper part). For each configuration, we recorded an ILS according to the procedure outlined in Sect. 2.1. Fig. 5, lower part, shows the distortions of the ILS caused by inhomogeneous illumination. Clearly, we observe changes in the width and the peakedness of the ILS with narrower and more peaked ILS occurring when the lower part of the reflector plate was blocked. Note that the orientation of the image depends on viewing direction, since the image rotates with azimuth viewing direction.

We conclude that the ILS of the EM27/SCA is sensitive to scene heterogeneity. However, the checkerboard pattern used for the laboratory testing is certainly an extreme configuration. Thus, we expect the effect to be smaller for typical targets in the field. Nevertheless, we took care of selecting homogeneous targets for our field deployment in LA.

3 Field deployment at Los Angeles

To evaluate the performance of the EM27/SCA, we deployed it side-by-side with the CLARS-FTS during a period of roughly one month. We positioned the EM27/SCA adjacent to the CLARS-FTS on a small viewing terrace at the Mount Wilson observatory at $1670\,\mathrm{m}$ a.s.l. overlooking the Los Angeles basin (Fig. 1). We took measurements during 26 days in the period from Apr. 7, 2022, to May 5, 2022, pointing at up to 9 targets in the northern LA basin with slant distances of up to 25 km (see map in Fig. 6).

A typical measurement cycle started with a short-cut measurement of the reflector plate and then, cycled through the ground targets in the basin, including one additional short-cut measurement. We co-added 10 interferograms (at an interferogram sampling frequency of $10\,\mathrm{kHz}$) per target resulting in roughly $12\,\mathrm{min}$ duration for a full cycle of 9 ground targets plus 2 reflector measurements. In the later part of the campaign, we recorded 3 spectra per target, with 10 interferograms each, increasing the duration of a full cycle to $36\,\mathrm{min}$. The early phase of the campaign was dedicated to testing the setup and finding the best measurement configurations and therefore, on a few days, a cycle covered only a single or a few ground targets (instead of the total of nine) and one reflector measurement. On three days, we only conducted reflector measurements since a marine cloud layer covered the basin. Simultaneously with the spectrometer recording interferograms, the FOV-camera captured an image of each target scene in each cycle and the context-camera recorded an image of the overhead sky.
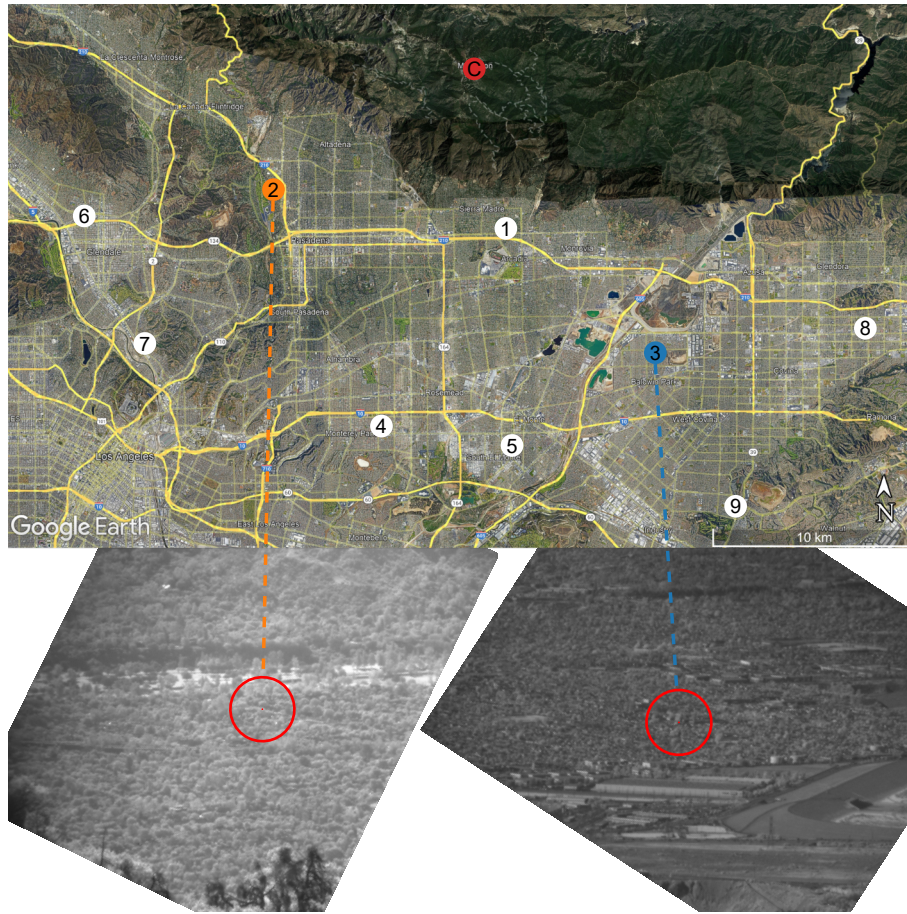
8

Figure 6. Location of the CLARS-FTS on Mt. Wilson (C) and ground scattering targets (numbers) in the LA basin. The lower panel shows FOV-camera images of the West Pasadena (WP) (2, left image) and Baldwin Park (BP) (3, right image) targets. The instrument FOV is marked in red.

The pointing directions for each target were determined at the start of the campaign via the FOV-camera of the CLARS-FTS. As discussed in Sect. 2.3, special care was taken that the target scenes were homogeneous i.e. not exhibiting strongly contrasted features across the FOV. However, in an urban setting, perfectly homogeneous targets are not available. GPS coordinates of the targets are available through the pointing calibration of the CLARS-FTS (Fu et al., 2014). After target selection, the EM27/SCA was pointed to the same targets as CLARS-FTS via direct comparison of the FOV images.

For our initial demonstrator assessment in Sect. 5, we focus on the two targets West Pasadena (WP) and Baldwin Park (BP), which have the most revisits. These targets represent urban ground with houses, as visible in Fig. 6. The targets have a slant distance of 11.5 km (WP) and 16.4 km (BP).
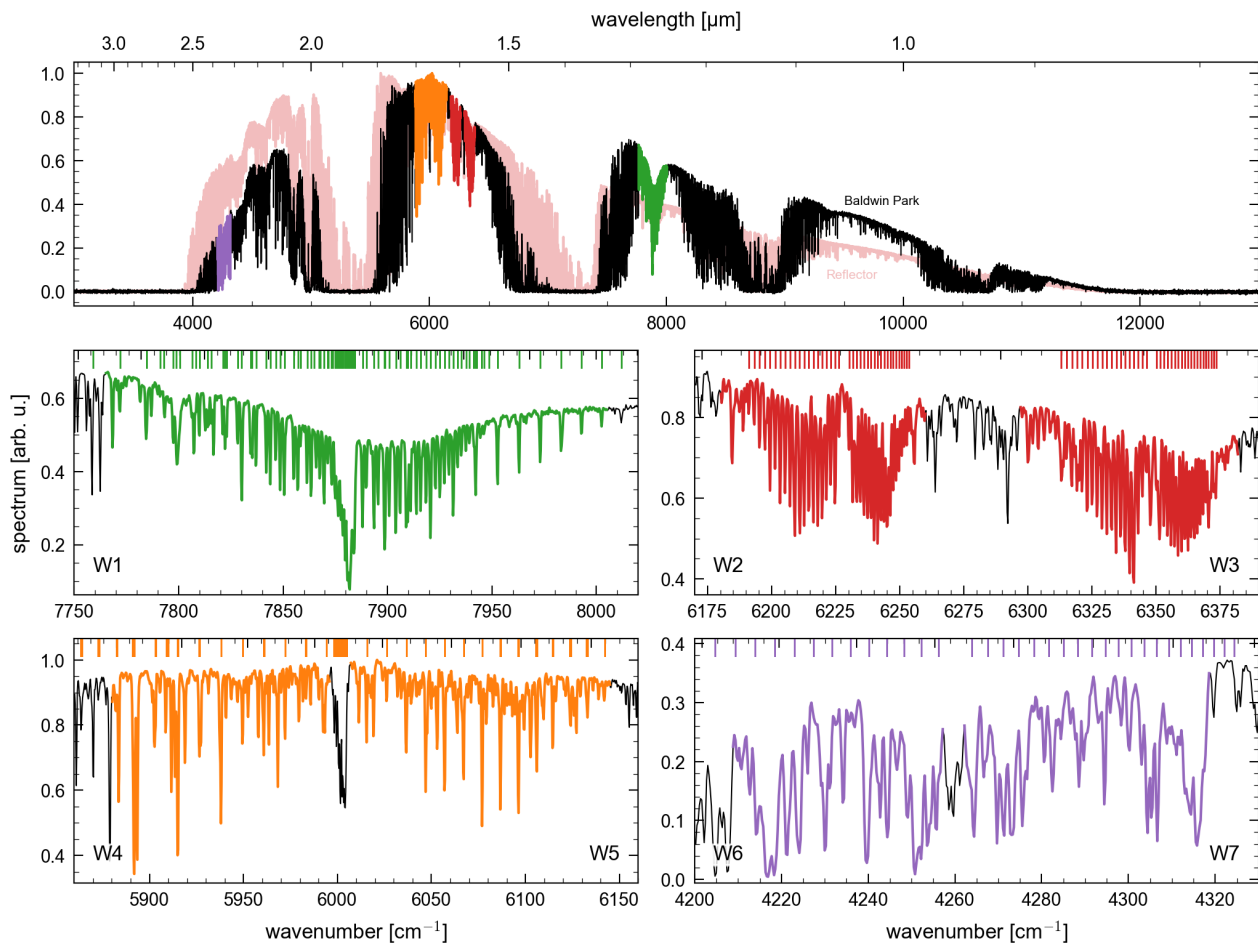
9

Figure 7. Typical reflected-sun spectrum of the BP target around 15:50 LT (at SZA 46.6°). The first panel shows the full spectrum with the retrieval windows highlighted in color. A reflector spectrum from roughly the same time is plotted in the background. The other panels show the retrieval windows for CO_2 (red), CH_4 (orange), CO (purple) and O_2 (green). Note that CO is a weak absorber and that W6 and W7 are dominated by CH_4 and H_2O absorption lines.

4 Spectral retrieval

The EM27/SCA recorded DC-coupled interferograms which we converted to absorption spectra via Fourier transform using the preprocessor of the PROFFIT retrieval software routinely employed for EM27/SUN processing within the COCCON network (Frey et al., 2019). Throughout this study, we used the Norton-Beer medium apodization. The processing included a DC correction that corrected the interferograms for mild brightness fluctuations during recording. Together with the spectra, we stored the height of the center burst of the interferograms as well as a measure for DC fluctuations. Later, we used this data to identify spectra suffering from cloud contamination and over-saturation.
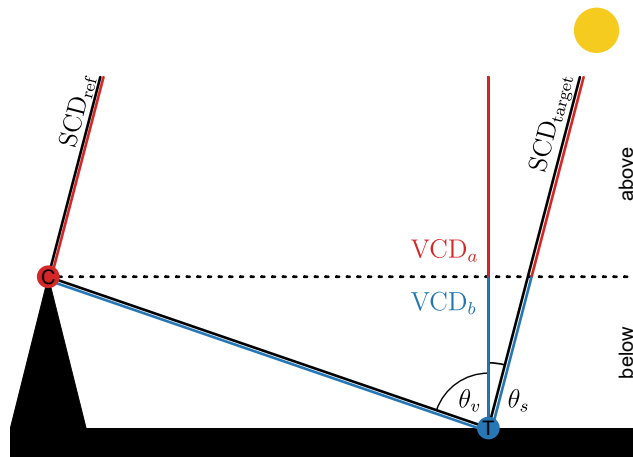
Figure 8. Representation of the viewing geometry as implemented in the retrieval. We separate the model atmosphere at instrument level, scaling the VCDs above in reflector and below in target retrievals. From the resulting VCDs we derive the total SCDs for reflector (SCD_{ref}) and target (SCD_{target}) measurement. Finally, we calculate VCD_a from SCD_{ref} and VCD_b from the difference between SCD_{ref} and SCD_{target} (see Eq. (3)).

Fig. 7 shows a typical absorption spectrum measured with the EM27/SCA and highlights the absorption bands used for the retrievals of CO_2, CH_4, CO and O_2. We submit the absorption spectra to a variant of the RemoTeC radiative transfer and retrieval algorithm to infer the gas abundances. RemoTeC has been designed for satellite measurements of XCO_2, XCH_4, and XCO in the SWIR spectral range (Butz et al., 2011). The variant we employed here has been modified to accommodate the particular observation geometry (see Fig. 8) by dividing the layered, horizontally homogeneous model atmosphere into an overhead part, i.e. the part of the atmosphere above the instrument stationed at Mt. Wilson, and a boundary layer part, i.e. the part of the atmosphere below the instrument where the targets in the LA basin are located. For the overhead part, the forward model calculates the one-way downward slant transmittance of sunlight at instrument level. For the boundary layer part, the forward model corresponds to the two-way transmittance between instrument level and the level of ground reflection taking into account the solar (SZA, θ_s) and the viewing zenith angles (VZA, θ_v). Combining the overhead and boundary layer transmittances yields the forward model simulating the expected measurements for the LA basin targets. For short-cut measurements of the reflector plate, only the overhead part is relevant.

We set up the retrieval such that a least-squares estimator delivered vertical column densities (VCDs) of the target absorbers. We regularized our retrieval such that each absorber had one degree of freedom in the vertical. For reflector measurements, we scaled the overhead VCDs. For target measurements, we varied the partial VCDs in the boundary layer part, while the overhead part was imposed by the a priori. The following performance analysis makes further use of slant column densities (SCDs) defined as

$$SCD = VCD \times AMF \tag{1}$$

11

where AMF is the air mass factor, the ratio of the slant path through a layer to the vertical depth of the layer. As such, the AMF is different for the parts above (AMF_a) and below (AMF_b) instrument level. They are defined via

$$AMF_a = \frac{1}{\cos(\theta_s)}, \quad AMF_b = \frac{1}{\cos(\theta_s)} + \frac{1}{\cos(\theta_v)} \tag{2}$$

under our geometric assumptions (c.f. Fig. 8). Analyzing the SCDs is useful, because they directly relate to optical thickness, and with it to the spectra, making them a good quantity for the performance evaluation of the EM27/SCA.

VCDs offer the advantage that geophysical variation is deconvolved from changes in the geometric lightpath. However, they incorporate geometric assumptions, which in our case differ above and below instrument level (c.f. Eq. (2)). This non-uniformity throughout the model atmosphere makes total VCDs difficult to interpret, because an increase in the SCD below instrument level has a much smaller effect on the VCD than the same increase in the SCD above instrument level. To circumvent this problem, we evaluated the partial VCDs above (VCD_a) and below (VCD_b) the instrument separately. VCD_a are directly calculated from the reflector measurements. VCD_b are derived from the differences between the SCDs from the target (SCD_{target}) and the reflector (SCD_{ref}), taking into account AMF_b.

$$VCD_a = \frac{SCD_{ref}}{AMF_a}, \quad VCD_b = \frac{SCD_{target} - SCD_{ref}}{AMF_b} \tag{3}$$

To calculate VCD_b, we interpolated SCD_{ref} between reflector measurements bracketing the time of the target measurement. VCD_b is the quantity ultimately of interest and also the quantity our target measurements are most sensitive to.

Note that, for the initial assessment of the instrument performance, we did not consider scattering by particles in the forward model, as also previously assumed by Fu et al. (2014). This is also the basis for our choice of regularization described above. While we scale the vertical absorber profile for reflector measurements, for target measurements we expect the largest variability below instrument level. For one, this layer contains a large portion of the lightpath and the emission signal we aim at. Secondly, variability due to unaccounted aerosol scattering originates there (c.f. Fig. 14 and the discussion in sections 5.3 and 6). Thus, it is reasonable to attribute all variability to the lowest layer rather than scale the total column. Especially, since we only use total SCDs in the further analysis (c.f. Eq. (3)), errors in the a priori profile above instrument level are compensated for in the lowest layer. The remaining error is caused by attributing the molecules in the total column to regions with different pressure and temperature. We summarize the retrieved parameters and assumptions in table 1.

Table 2 lists the spectral windows (see also Fig. 7) from which we retrieved the O_2, CO_2, CH_4 and CO VCDs. Absorption cross sections for all species were calculated from spectroscopic parameters using a Voigt line shape and the HITRAN 2020 database (Gordon et al., 2022). In W1 we include a pseudo absorber accounting for the O2 collision induced absorption (CIA). All absorbers were retrieved independently for each window. Note that windows W4 and W5 excluded the CH_4 Q-branch, as we found systematic errors in retrievals including it. For windows W6 and W7, we found that retrieving the main H_2O isotopologue and HDO independently reduced fitting residuals. In all other windows the H_2O cross sections included lines of all isotopologues scaled with their standard abundance. Broad band variation of the spectrum baseline was accounted for through fitting a spectral background polynomial together with the gas VCDs. Since we neglect aerosol scattering, the polynomial represents the scene brightness, but is not strictly the surface albedo. The polynomial is of 4th order in W2 to W7

12

Table 1. Overview of retrieved and assumed parameters, detailed description in the main text.

parameter	description
Retrieve	
Absorber column density*	*reflector*: scaling of the vertical profile
	target: scaling of the partial column below instrument level
Spectral background polynomial	polynomial of order 5 (W1) or 4 (W2-W6)
Spectral shift	linear spectral shift of the measured spectrum and of the solar
	spectrum with respect to the absorption cross sections
Assume	
Absorption cross sections	Voigt lineshape with parameters from HITRAN 2020
Instrument line shape	as described in Sect. 2.1
No aerosol scattering	no particle scattering in the atmosphere, see discussion in Sect.
	5.3 and 6
Model atmosphere	Plane parallel model atmosphere
Viewing geometry	as shown in Fig. 8 with AMF according to Eq. (2)
A priori vertical profile	CarbonTracker 2019 (CO_2), TM4 (CH_4, CO) and NCEP (H_2O
	and O_2 from pressure)

*absorbers are listed in table 2

Table 2. Retrieval windows

ID	spectral range [cm^{-1}]	width [cm^{-1}]	absorber target	interfering	BG
W1	7765 – 8005	240	O_2	H_2O, O_2 CIA	5
W2	6180 – 6260	80	CO_2	H_2O	4
W3	6297 – 6382	85	CO_2	H_2O	4
W4	5880 – 5996	116	CH_4	H_2O	4
W5	6007 – 6145	138	CH_4	H_2O, CO_2	4
W6	4208.7 – 4257.3	48.6	CO	H_2O, HDO, CH_4	4
W7	4262.0 – 4318.8	56.8	CO	H_2O, HDO, CH_4	4

BG: spectral background polynomial order

and 5th order in the largest window W1. We computed the solar spectrum from the empirical line list by Toon (2015), which was also used by Coddington et al. (2021) for the computation of the TSIS-1 HSRS.

225   RemoTeC used a priori profiles from CarbonTracker 2019 (Jacobson et al., 2020) for CO_2 and TM4 (Meirink et al., 2006) for CH_4 and CO. Water vapor (H_2O) and oxygen (O_2) a priori profiles were calculated from NCEP meteorological data (NCEP,

2000), which also provided the vertical pressure and temperature profiles. The pressure at instrument level was taken from the CLARS weather station (Fu et al., 2014) and was used as the lowest pressure level for the reflector measurements as well as for dividing the atmosphere in the overhead and boundary layer part in the case of the target measurements.

230   To exclude unreliable measurements, we applied a series of filters to all measurements. We did not analyze spectra recorded at SZA greater than $70°$, and filtered measurements with signal-to-noise ratio (SNR, defined in Sect. 5) less than 100 in W1–W5 and less than 50 in the CO retrieval windows. Only few measurements were removed due to low SNR in W1–W5 (0.2%), while 4% of the measurements were excluded from CO retrievals in W6 and W7. Additionally, the CO retrieval did not fully converge for 18% of the measurements. These measurements were still used for retrievals of species from the other windows.

235   We further filtered for cloud contamination by utilizing the DC component of the interferogram, as proposed by Klappenbach et al. (2015). Since the DC component changes with temporal variations in sunlight intensity, its variability increases when the sun is partially obstructed. We calculated the variability DC_{var} as the fraction of maximum (DC_{max}) to minimum (DC_{min}) value of the baseline and subtracted one so that no variability corresponds to a value of zero.

$$DC_{var} = \frac{DC_{max}}{DC_{min}} - 1 \tag{4}$$

240   The cut-off value of this filter was empirically determined to 0.03 from cloud free measurements, identified with the help of the context camera. 7% of the measurements were removed by this filter.

5   Performance

5.1   Signal-to-noise and spectral residuals

To evaluate the performance of the EM27/SCA, we start with calculating the spectral SNR for the retrieval windows defined

245   in table 2 and illustrated in Fig. 7. The SNR is the ratio of the maximum transmittance in the respective window over the out-of-band noise. The latter was calculated as the standard deviation in the spectral range 2500–3056 cm^{-1}, where there is zero throughput of the spectrometer system. Generally, the SNR depends on multiple factors including the spectrally variable optical throughput, sensitivity of the detector, reflectivity of the target, spectral solar irradiance, position of the sun in the sky, and atmospheric conditions. Fig. 9 shows the SNR in dependence of SZA for spectra of the reflector and the two targets BP

250   and WP.

Typical SNR values range from 200–400 for target and 400–600 for reflector measurements. The SNR for the reflector measurements is most compact and follows a clear dependence on SZA since these measurements, being conducted at high elevation and having zero horizontal path, approximate direct sun conditions. The SNR of the target measurements shows more scatter and no compact SZA dependency, which points at a strong influence of atmospheric conditions, atmospheric scattering

255   effects and the geometry of surface structures. For the O_2 window (W1), the generally greater surface reflectivity compensates for the reduced detector sensitivity compared to the CO_2 (W2, W3) and CH_4 windows (W4, W5) of the targets. The CO retrieval windows (W6, W7) exhibit lower SNR on the order of 50–150, as the windows are located towards the longwave

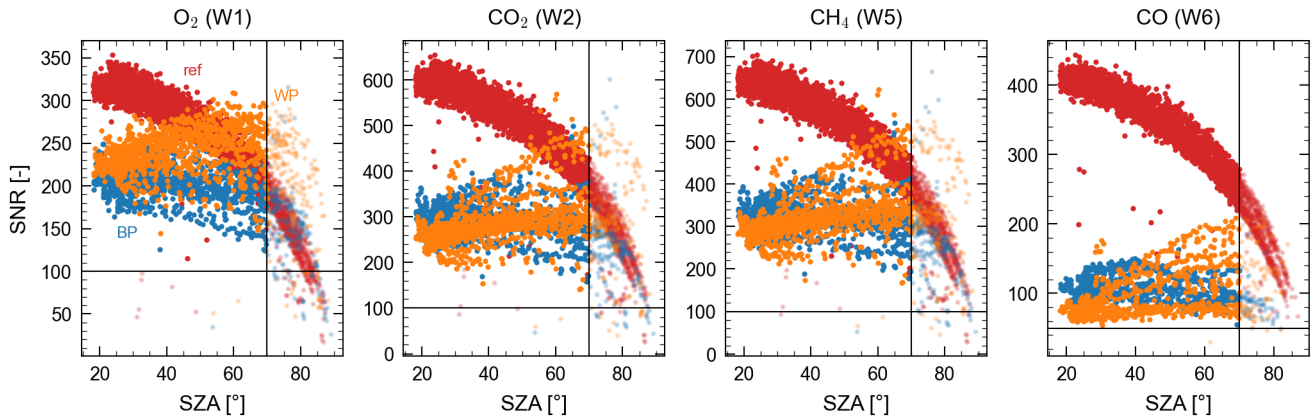**14**

Figure 9. SNR for spectra measured between Apr. 7 and May 5, 2022 plotted against SZA for the reflector (red), and the targets BP (blue) and WP (orange).

cut-off of the InGaAs detector. Note that SNR in the CO retrieval windows is generally lower for WP than for BP. We attribute the upward SNR trends with increasing SZA for WP to atmospheric scattering towards the evening.

260   Processing the acquired spectra with RemoTeC (see Sect. 4) yields best-fit simulated spectra. They allow for inspecting the spectral fitting residuals, defined as the differences between the measured spectra and the best-fit simulations. Fig. 10 shows the spectral residuals for one window of each species, averaged over a whole day of observations. For averaging, each residual was normalized by the maximum measurement signal in the respective window. Due to the averaging, noise is negligible and the spectral residuals reveal systematic errors due to deficiencies in the retrieval simulations, such as forward model approximations

265   and parameter errors. The residuals and their root-mean-square (RMS) for the reflector measurements are generally smaller than for the targets in the LA basin. This points at contributions from the neglect of atmospheric scattering, which is a better approximation for the reflector than for the target measurements. Further, spectroscopic uncertainties, such as line shape errors, typically grow with the length of the lightpath, as absorption lines become more opaque and thus target spectra might be more affected than the reflector measurements. Individual spectral structures correlate with the positions of H_2O lines (e.g. at 5892,

270   5940, 6020, 6226, 6242, 6305, 6325, 6334 and $6363 \, \mathrm{cm}^{-1}$), suggesting spectroscopic errors. The fitting residuals in the O_2 window (W1) are larger and more systematic than for CO_2 (W2, W3) and CH_4 (W4, W5). Despite revisiting our calibration procedures, taking into account spectral variation of the ILS and performing various sensitivity runs, we were not able to identify the cause for this.

     Fig. 11 evaluates the RMS of the spectral residuals against SNR. Generally, the RMS follows the 1/SNR pattern expected

275   from a noise-dominated measurement for both reflector and target spectra. However, there is an offset that comes from the systematic residual structures which are particular pronounced in the O_2 band.
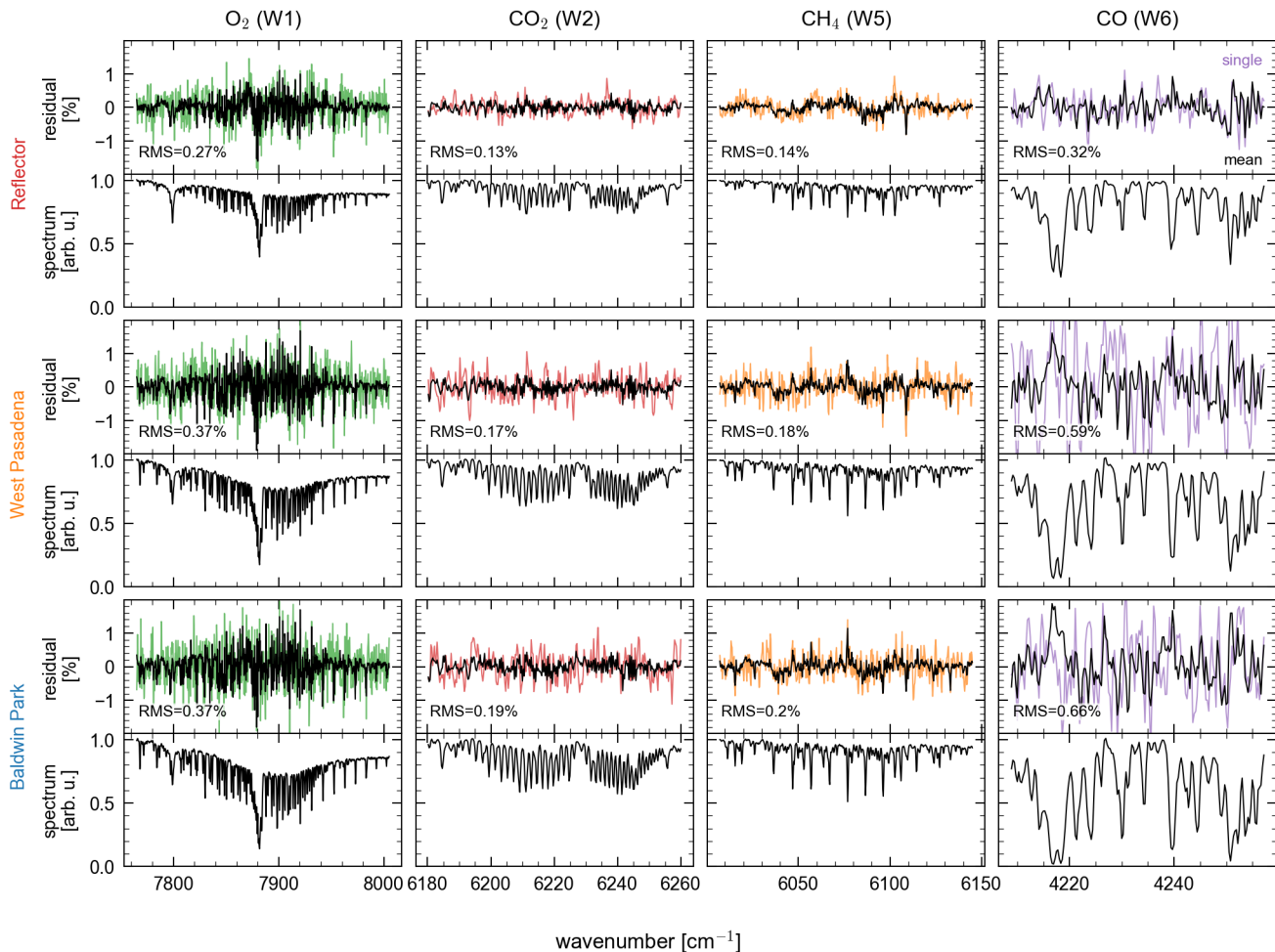
15

Figure 10. Spectra and spectral residuals for the reflector (upper row), target WP (middle row) and target BP (lower row) for the W1 (O_2, green, first column), W2 (CO_2, red, second column), W5 (CH_4, orange, third column) and W6 (CO, purple, fourth column) windows. The lower subplots in each panel show a single spectrum; the upper subplots show a residual from the single spectrum (colored) and a full day average (black) of 124 (reflector), 124 (WP), and 122 (BP) normalized residuals (119, 112 and 112 for CO).

Overall, the spectral performance of the EM27/SCA is promising in terms of retrieving precise CO_2, CH_4 and O_2 columns. For CO, the spectral cut-off of the detector and the low surface reflectivity around $4250\,\mathrm{cm}^{-1}$ imply small SNR. A next-generation instrument might consider detectors and optics with better performance at the longwave end of the SWIR.

5.2 Precision

To estimate the measurement precision we empirically evaluate the precision of the retrieved SCDs for each gas (as explained in Sect. 4). We evaluated 4 days of measurements from the early campaign period, where the sampling of the evaluation targets
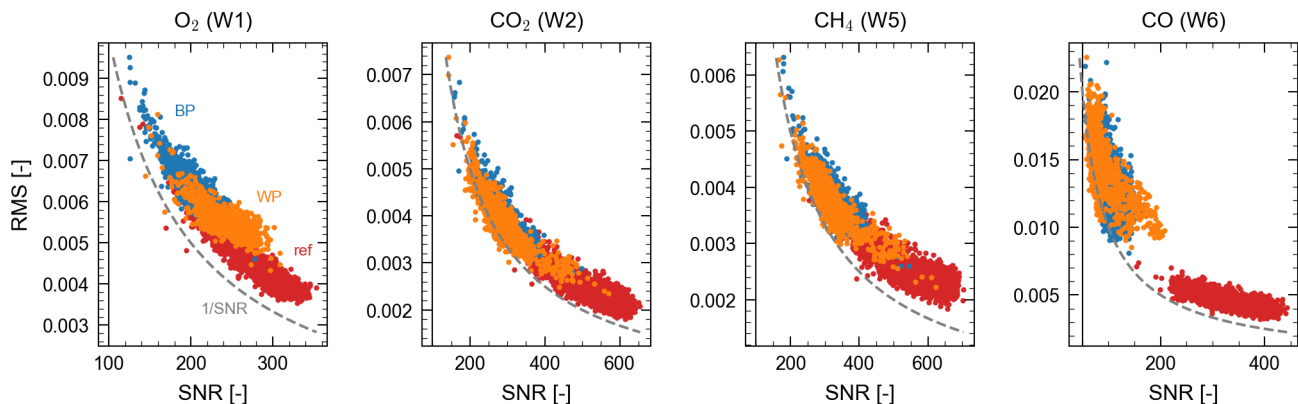
Figure 11. RMS of the spectral residuals for measurements between Apr. 7 and May 5, 2022 plotted against SNR for the reflector (red) and the BP (blue) and WP (orange) targets.

Table 3. Relative precision error of the absorber SCDs estimated from the departures of individual measurements from a 30 min rolling average. Numbers in parentheses show the last digit changes when repeating the analysis with 20 min and 40 min rolling averages.

	window	reflector N = 334	WP N = 409	BP N = 363
O_2	W1	0.49(1)%	0.40(3)%	0.51(5)%
CO_2	W2, W3	0.36(2)%	0.41(3)%	0.39(3)%
CH_4	W4, W5	0.50(2)%	0.55(4)%	0.49(5)%
CO*	W6, W7	7.5(4)%	15.6(9)%	8.7(5)%

*N is lower for CO retrievals: 261 (reflector), 177 (WP), 232 (BP)

was densest. We calculated the precision error as the standard deviation σ of the ratio between each measurement and a rolling average,

$$\Delta\mathrm{SCD} = \sigma\left(\frac{\mathrm{SCD}_i}{\langle\mathrm{SCD}\rangle_t}\right) \tag{5}$$

where $\Delta\mathrm{SCD}$ is the estimated relative precision error of the SCDs, SCD_i is the slant column density of measurement i, and $\langle\mathrm{SCD}\rangle_t$ is the rolling average SCD. We chose an averaging interval of $t = 30$ min, corresponding to 7 measurement cycles, as a trade-off between convolving actual geophysical variability into our precision estimates and considering a sufficient number of samples for calculating the average SCDs. Fig. 12 shows the ratio of the SCDs to their rolling average against SZA, as well as the histograms. Table 3 lists the resulting relative precision errors for the various absorbers. For CO_2, CH_4 and O_2 SCDs we find a relative precision of 0.36–0.55% without a distinct dependency on SZA. The precision for CO SCDs is considerably worse, as expected from the low SNR in windows W6 and W7 and the weakness of the CO absorption signal. To test the
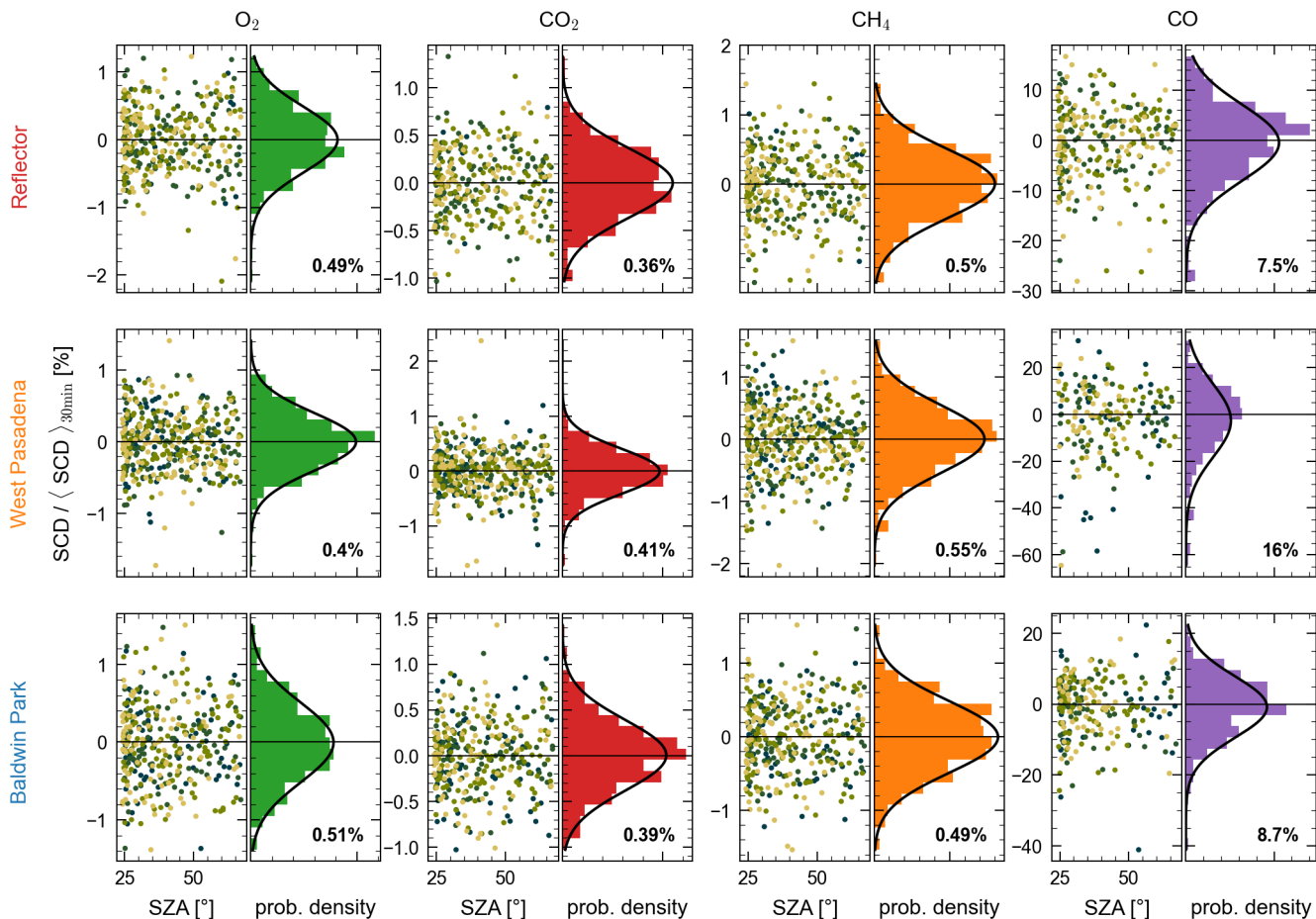
Figure 12. Departures of O_2, CO_2, CH_4 and CO (columns left to right) SCDs from their 30 min rolling average, plotted against SZA (left subpanels) and as histograms (right subpanels) including a normal distribution with the corresponding mean and standard deviation for the reflector (upper row) and the WP (middle row) and BP (lower row) targets. The scatterplots are color coded by day.

robustness of these estimates, we repeated the analysis with rolling averages over 20 min (5 cycles) and 40 min (9 cycles), which resulted in only small changes (table 3).

295 5.3 Comparison to CLARS-FTS

To assess the consistency of the EM27/SCA measurements to those of CLARS-FTS, we submitted the CLARS-FTS spectra of the same targets WP and BP and CLARS-FTS' own reflector to the RemoTeC retrieval with analogue settings as for the EM27/SCA spectra. We interpolated the higher precision CLARS-FTS partial VCDs in time to EM27/SCA measurement
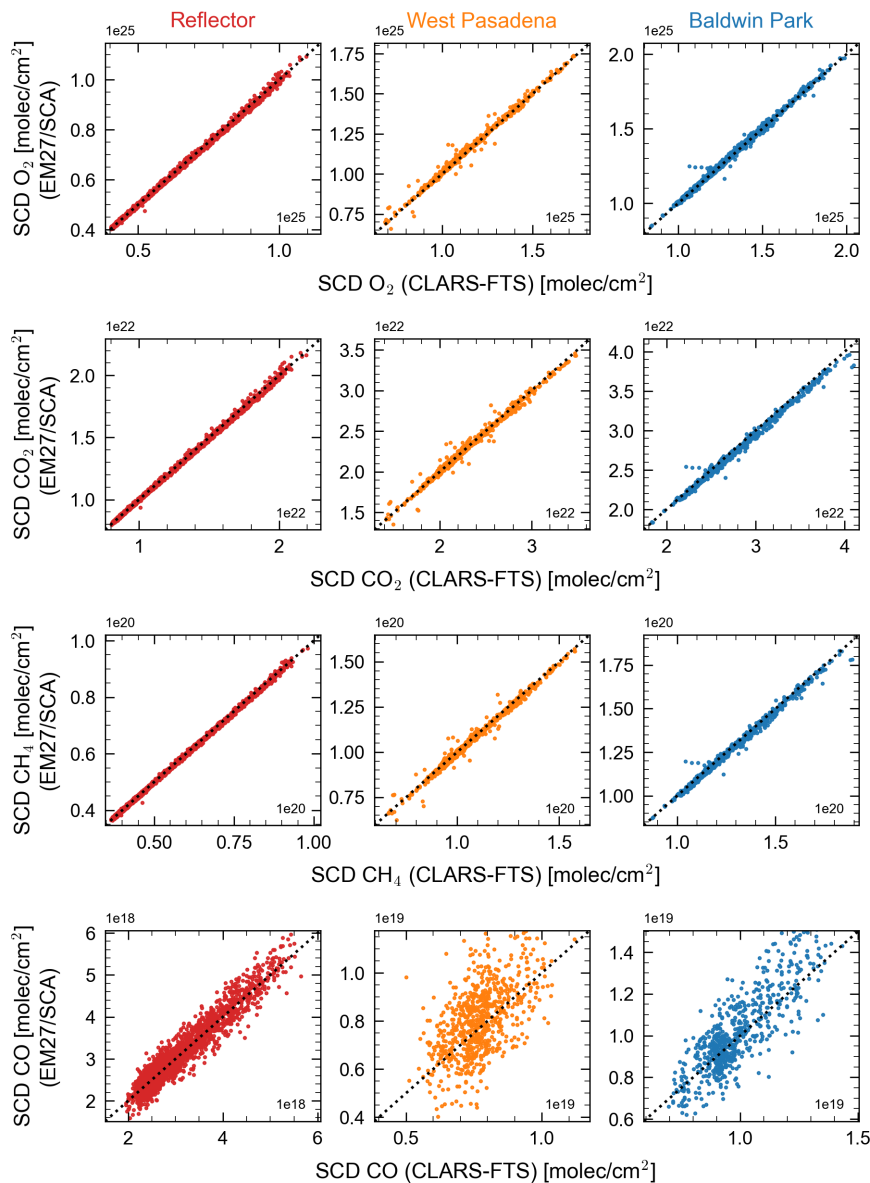
18

Figure 13. Correlation of O_2, CO_2, CH_4 and CO SCDs (top to bottom row) between EM27/SCA and CLARS-FTS for reflector (red, left), WP (orange, middle) and BP (blue, right) measurements. The dotted lines show the 1:1 relationship.

instances, and subsequently calculated the CLARS-FTS SCDs. Evaluating all the reflector measurements in the campaign period, we found that CLARS-FTS SCDs differ from EM27/SCA SCDs on average by a factor 1.046 for O_2, 1.0068 for CO_2, 1.014 for CH_4 and 0.997 for CO. Such scaling factors might originate from the different spectral resolutions of the EM27/SCA

$(0.56\,\mathrm{cm}^{-1})$ and the CLARS-FTS $(0.2\,\mathrm{cm}^{-1})$ as Gisi et al. (2012) found for TCCON to EM27/SUN comparisons. For all the following analyses, we scaled the EM27/SCA retrievals by these factors.

Fig. 13 shows the correlation between the EM27/SCA and CLARS-FTS retrievals. Measurements of the reflector and both targets show a good correlation in O_2, CO_2 and CH_4 with correlation coefficients near 1. CO shows a decent correlation for reflector measurements. For target CO measurements the low precision dominates.

Fig. 14 shows the observed diurnal variations of the O_2, CO_2, CH_4 and CO partial VCDs above (VCD_a) and below (VCD_b) instrument level for the EM27/SCA and CLARS-FTS for three illustrative days. We calculate the precision error of the partial VCDs via Gaussian error propagation from the relative precision of target and reflector SCDs (table 4). Since the fraction of the light path below instrument level depends on target distance and SZA, the precision error for target measurements increases for closer targets and higher SZA.

Focusing on the overhead reflector measurements first (red symbols in Fig. 14), we find that the two instruments generally agree well for all four absorbers and that the VCD_a are not much variable during the day and from day-to-day as expected for the quasi-direct sun geometry. Generally, the CLARS-FTS has substantially better precision than the EM27/SCA as expected from the CLARS-FTS evaluation by Fu et al. (2014). The standard deviations of the differences between EM27/SCA and CLARS-FTS VCD_a amount to 1% for O_2, CO_2 and CH_4 respectively, and 7% for CO. There are some systematic deviations, especially in the early morning hours, for CO_2 and, although weaker, also for O_2 and CH_4. For these species, the EM27/SCA records show a low bias on Apr. 13, and on May 5 there is a diurnal variation on the order of the precision error, which is not present in the CLARS-FTS data. For CO, the large scatter masks possible systematic differences.

Turning the focus to the VCD_b in the boundary layer below instrument level (orange and blue symbols in Fig. 14), we generally find that O_2, CO_2 and CH_4 show strong diurnal variations with amplitudes exceeding 10% of the VCD_b. These variations are present in O_2 and strongly correlated between species, thus pointing to the influence of light scattering by aerosols. Since aerosol scattering effects are unaccounted for in our retrieval, the presence of aerosols implies a forward model error that shows up as VCD underestimation if scattering induces lightpath shortening and vice versa for lightpath enhancement compared to our geometric lightpath assumption. While these atmospheric scattering effects have large implications for how to interpret the data (Zhang et al., 2015), the VCD_b from EM27/SCA and the CLARS-FTS are largely consistent. For the BP target (blue symbols in Fig. 14), there are systematic deviations of the EM27/SCA records from the CLARS-FTS data e.g. on Apr. 13 for O_2 in the evening and for CO_2 in the morning, and on Apr. 14 for CO_2 throughout the day. These systematic deviations are less pronounced for the WP target. After extensive sensitivity studies, we speculate that scene heterogeneity for the BP target may contribute to these deviations. Scene heterogeneity can be variable during the day due to the changing illumination conditions of the ground scene. As explained in Sect. 2.1, heterogeneous illumination of the target affects the ILS of the EM27/SCA, which in turn induces errors in the gas retrievals if the ILS distortion is not accounted for. Due to the lower spectral resolution of the EM27/SCA, the effect on the retrievals is larger than for the CLARS-FTS since the overall impact of the ILS is larger for low than for high resolution.
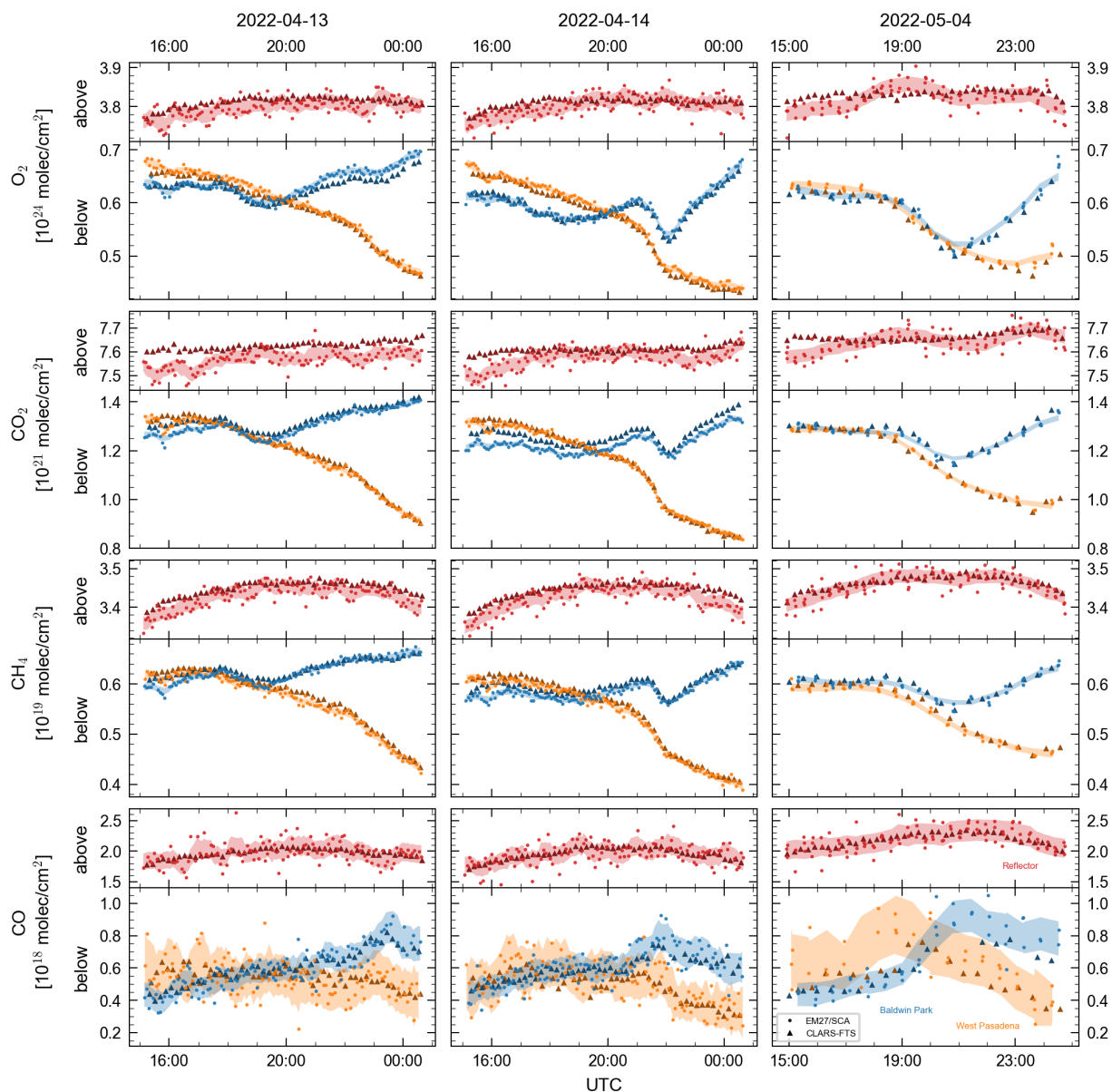
Figure 14. Timeseries of the VCD_a (above) and VCD_b (below instrument level) of O_2, CO_2, CH_4 and CO (top to bottom) measured by the EM27/SCA (dots) and the CLARS-FTS (triangles). Three illustrative days are shown left to right. The partial VCD_a is retrieved from reflector measurements (red). The VCD_b below is derived from the difference of WP (orange) and BP (blue) to the reflector measurement. The EM27/SCA precision error is displayed as shading around the rolling average. The first two days belong to the period where we cycled through three targets only, and therefore, these days show a higher sampling rate.

Table 4. Relative precision error range for VCD_a and VCD_b on Apr. 13.

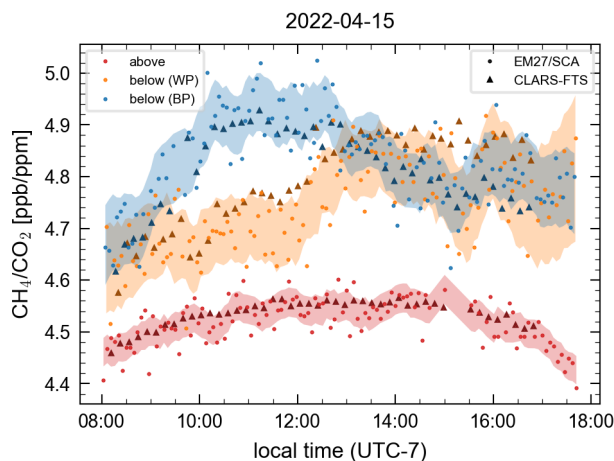|	VCD_a	VCD_b	
		WP	BP
O_2	0.49%	0.77–1.6%	0.85–1.3%
CO_2	0.36%	0.75–1.5%	0.64–0.99%
CH_4	0.50%	0.98-2.0%	0.79–1.2%
CO	7.5%	20–44%	11–18%

Figure 15. Single day of CH_4/CO_2 ratio measurements show a CH_4 enhancement in the Los Angeles basin assuming a constant CO_2 background (Wong et al., 2015).

6   Discussion and conclusion

Our study discusses the prototype design and performance of the EM27/SCA FTS. The instrument concept is based on the direct-sun EM27/SUN FTS, but it achieves manifold higher sensitivity making it suitable for measurements of sunlight reflected by ground targets of opportunity. While being portable, the instrument mimics the observation concept of the CLARS-FTS stationed at Mt. Wilson looking downward into the LA basin. Our performance evaluation during a month-long side-by-side deployment with the CLARS-FTS shows that the precision errors for the SCDs of CO_2, CH_4, and O_2 retrieved from EM27/SCA measurements are on the order of 0.5%, which translates into errors of 0.7 to 2% for the partial VCDs in the layer below instrument level (VCD_b) in the LA basin, somewhat depending on the ground reflection target. For CO, precision errors for the SCDs are in the range from 7 to 16%, translating into errors of several ten percent for the VCD_b of the targets in the LA basin. Thus, while performance is promising for detecting urban enhancements of CO_2 and CH_4, the EM27/SCA requires reduction of the noise level in the CO channel (around 2.350 nm).

As previous studies for CLARS-FTS (Zhang et al., 2015; Zeng et al., 2017) and our Fig. 14 show, the particular viewing geometry, with a long horizontal lightpath component exceeding $10\,\mathrm{km}$ through the urban boundary layer of LA, causes light scattering by aerosols to be the dominant source of variation in the retrieved VCD_b, if aerosol effects are neglected in the gas retrievals. To correct to first order for these scattering effects, the column averaged dry-air mole fractions X_i of gas i can be calculated via

$$\mathrm{X}_i = \frac{\mathrm{SCD}_i}{\mathrm{SCD}_{\mathrm{REF}}} \times \mathrm{X}_{\mathrm{REF}} \tag{6}$$

where REF denotes a reference gas whose dry-air mole fraction $\mathrm{X}_{\mathrm{REF}}$ is known a priori. The idea is that aerosol scattering effects induce the same relative errors in the spectral retrievals of species i and REF and thus, the effects cancel in Eq. (6). Using O_2 as a reference gas is appealing since its dry-air mole fraction is well known and constant for all relevant purposes here. However, Zhang et al. (2015) show that using O_2 as reference gas results in erroneous corrections since the $O_2\Delta$ band is spectrally distant from the retrieval windows of the target gases CO_2, CH_4 and CO. Thus, spectral variation of the aerosol and ground scattering properties make the radiative transfer in the O_2 windows different from the other windows. In contrast, ratioing CH_4 with CO_2 from the neighboring spectral windows better compensates for the radiative transfer effects. Fig. 15 illustrates a case where the CH_4/CO_2 ratio for BP in the morning has a substantial enhancement compared to the data for WP and the reflector. The NOAA High-Resolution Rapid Refresh dataset (Dowell et al., 2022) indicates south-west to west wind conditions at windspeeds increasing from 1 to $5\,\mathrm{m/s}$ over the course of the day. Following the studies for CLARS-FTS (Wong et al., 2015, 2016), we argue that this is a geophysical signal related to emission and transport patterns in the LA basin. Major CH_4 point sources are located south west of the BP target (see Fig. A1). However, in order to relate the CH_4/CO_2 patterns to CH_4 emissions and their transport, according to Eq. (6), we would require assumptions on the reference XCO_2. Additionally, source attribution would require atmospheric transport modelling. We tentatively identify the increase in the CH_4/CO_2 ratio around 12:00 to 13:00 hours local time for the West Pasadena target also in TCCON measurements at CalTech (Wunch et al., 2011; Wennberg et al., 2022) (see Fig. A2), located $5\,\mathrm{km}$ south of the WP target. The magnitude of the CH_4/CO_2 signal differs substantially so that despite the high precision of the TCCON measurements, the signal is in the same order as the scatter. While the scatter in the EM27/SCA data is significantly larger, the signal is clearly observable. This illustrates the value of the reflected sunlight measurement geometry.

The usage of the CH_4/CO_2 ratio has been discussed in depth for the CLARS-FTS measurements (Wong et al., 2015, 2016; He et al., 2019; Zeng et al., 2023) and, we will follow up on such cases in future studies. Furthermore, we plan to develop a simultaneous retrieval of GHGs, aerosol properties and surface albedo. For this, we will need (1) an absolute calibration of the spectra and (2) adjustments to our radiative transfer model. Despite RemoTeC being able to retrieve aerosol properties in the satellite viewing geometry with the observer on top of the atmosphere, the radiative transfer model is not flexible enough to achieve this for an observer inside the atmosphere. Overcoming this limitation is in principle possible, but a major effort and out of scope for this instrument performance evaluation. Additionally, polarization effects could become important. If they have a significant impact on our retrieval, we need to account for the EM27/SCA polarization sensitivity and make an assumption on the polarizing properties of the surface. We will follow up on this in future studies.

380   Assuming that atmospheric scattering effects can be reliably corrected, the VCD_b errors listed in table 4 and shown in Fig. 14 directly yield a limit for detectable enhancements of the respective gas abundances in the LA basin. Verhulst et al. (2017) found typical local enhancements in the LA boundary layer in the range of 17-31 ppm CO_2 and 140-220 ppb CH_4. Zhang et al. (2015) estimated 10–20 ppm XCO_2 enhancements for CLARS-FTS measurements of the WP target by calculating the differences between CLARS-FTS spectralon and LA TCCON measurements. Zeng et al. (2021) showed typical enhancements

385 of 20 ppm in XCO_2 and 150 ppb in XCH_4 retrieved from CLARS-FTS measurements with the GFIT3 full physics algorithm. Assuming background mole fractions of 420 ppm for CO_2 and 1900 ppb for CH_4, these typical enhancements amount to relative variations of 5% (CO_2) and 8% (CH_4), and thus, they are greater than our VCD_b errors. If they occur in a correlated pattern, e.g. due to transport effects such as shown in Fig. 15, the EM27/SCA is able to reliably measure them.

    Our analysis suggests further refinements of the instrument. Enhancing signal-to-noise would be required for useful CO

390 measurements, and it would be generally beneficial for more reliable measurements and lower detection limits for all the gases. Section 2.1 highlights that the alignment of the detector optics is cumbersome and that the ILS is somewhat asymmetric, which we mainly relate to the detector optics being optimized for throughput, accepting inferior focusing quality as trade-off. Further, we find that the ILS of the EM27/SCA is sensitive to inhomogeneous illumination of the FOV (Sect. 2.1) and in Sect. 5, we speculate that residual systematic differences between the EM27/SCA and CLARS-FTS might be related to scene

395 inhomogeneity. Thus, a next generation instrument should consider improved detector optics and homogenizing the FOV.

    The largest potential for improvement lies in the explicit integration of aerosol scattering in the retrieval algorithm, as shown by Zeng et al. (2021). This would most likely improve fit quality, reduce uncertainty and pave the way to reliable measurements of near-ground CO_2 and CH_4 concentrations.
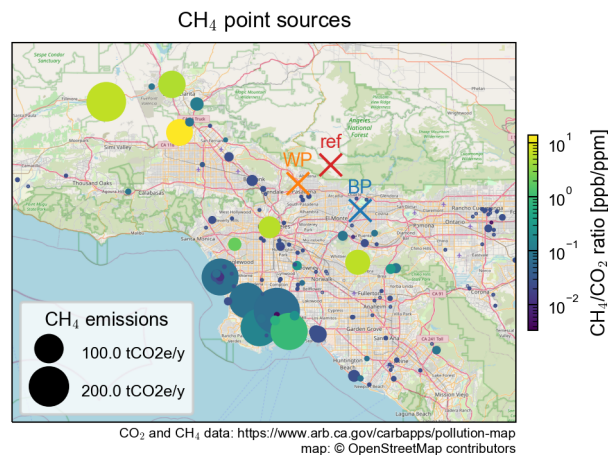
Figure A1. CH_4 point sources as registered in the California Air Resources Board inventory (CARB, 2000). Point size signals CH_4 emission strength, color corresponds to the CH_4/CO_2 emission ratio for the respective CH_4 source.
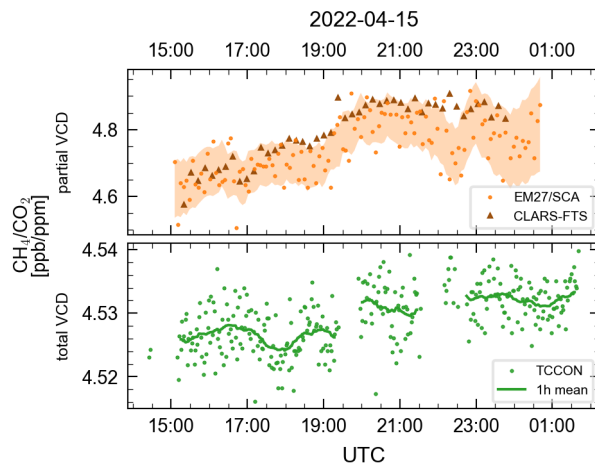

Figure A2. CH_4/CO_2 ratio between partial VCD below instrument level (upper panel, as in Fig. 15) measured with EM27/SCA (orange dots) and CLARS-FTS (orange triangles), and total VCD measured by TCCON at CalTech, Pasadena (lower panel, Wennberg et al. (2022)).

410

References

Addington, O., Zeng, Z.-C., Pongetti, T., Shia, R.-L., Gurney, K. R., Liang, J., Roest, G., He, L., Yung, Y. L., and Sander, S. P.: Estimating Nitrous Oxide (N2O) Emissions for the Los Angeles Megacity Using Mountaintop Remote Sensing Observations, Remote Sens. Environ., 259, 112 351, https://doi.org/10.1016/j.rse.2021.112351, 2021.

415 Board, C. A. R.: CARB Pollution Mapping Tool v2.6, https://www.arb.ca.gov/carbapps/pollution-map.

Butz, A., Guerlet, S., Hasekamp, O., Schepers, D., Galli, A., Aben, I., Frankenberg, C., Hartmann, J.-M., Tran, H., Kuze, A., Keppel-Aleks, G., Toon, G., Wunch, D., Wennberg, P., Deutscher, N., Griffith, D., Macatangay, R., Messerschmidt, J., Notholt, J., and Warneke, T.: Toward Accurate CO 2 and CH 4 Observations from GOSAT, Geophys. Res. Lett., 38, n/a–n/a, https://doi.org/10.1029/2011GL047888, 2011.

420 Butz, A., Dinger, A. S., Bobrowski, N., Kostinek, J., Fieber, L., Fischerkeller, C., Giuffrida, G. B., Hase, F., Klappenbach, F., Kuhn, J., Lübcke, P., Tirpitz, L., and Tu, Q.: Remote Sensing of Volcanic CO2, HF, HCl, SO2 and BrO in the Downwind Plume of Mt. Etna, Atmos. Meas. Tech., 10, 1–14, https://doi.org/10.5194/amt-10-1-2017, 2017.

Christen, A.: Atmospheric Measurement Techniques to Quantify Greenhouse Gas Emissions from Cities, Urban Climate, 10, 241–260, https://doi.org/10.1016/j.uclim.2014.04.006, 2014.

425 Coddington, O. M., Richard, E. C., Harber, D., Pilewskie, P., Woods, T. N., Chance, K., Liu, X., and Sun, K.: The TSIS-1 Hybrid Solar Reference Spectrum, Geophys. Res. Lett., 48, e2020GL091 709, https://doi.org/10.1029/2020GL091709, 2021.

de Foy, B., Schauer, J. J., Lorente, A., and Borsdorff, T.: Investigating High Methane Emissions from Urban Areas Detected by TROPOMI and Their Association with Untreated Wastewater, Environ. Res. Lett., 18, 044 004, https://doi.org/10.1088/1748-9326/acc118, 2023.

Dietrich, F., Chen, J., Voggenreiter, B., Aigner, P., Nachtigall, N., and Reger, B.: MUCCnet: Munich Urban Carbon Column Network, Atmos.
430 Meas. Tech., 14, 1111–1126, https://doi.org/10.5194/amt-14-1111-2021, 2021.

Dowell, D. C., Alexander, C. R., James, E. P., Weygandt, S. S., Benjamin, S. G., Manikin, G. S., Blake, B. T., Brown, J. M., Olson, J. B., Hu, M., Smirnova, T. G., Ladwig, T., Kenyon, J. S., Ahmadov, R., Turner, D. D., Duda, J. D., and Alcott, T. I.: The High-Resolution Rapid Refresh (HRRR): An Hourly Updating Convection-Allowing Forecast Model. Part I: Motivation and System Description, Weather and Forecasting, 37, 1371–1395, https://doi.org/10.1175/WAF-D-21-0151.1, 2022.

435 Duren, R. M. and Miller, C. E.: Measuring the Carbon Emissions of Megacities, Nature Clim. Change, 2, 560–562, https://doi.org/10.1038/nclimate1629, 2012.

Edenhofer, O., Pichs-Madruga, R., Sokona, Y., Farahani, E., Kadner, S., Seyboth, K., Adler, A., Baum, I., Brunner, S., Eickemeier, P., Kriemann, B., Savolainen, J., Schlömer, S., Stechow, v. C., Zwickel, T., and Minx, J. C.: IPCC, 2014: Climate Change 2014: Mitigation of Climate Change. Contribution of Working Group III to the Fifth Assessment Report of the Intergovernmental Panel on Climate Change,
440 Cambridge University Press, https://www.ipcc.ch/report/ar5/wg3/, 2014.

Frey, M., Hase, F., Blumenstock, T., Groß, J., Kiel, M., Mengistu Tsidu, G., Schäfer, K., Sha, M. K., and Orphal, J.: Calibration and Instrumental Line Shape Characterization of a Set of Portable FTIR Spectrometers for Detecting Greenhouse Gas Emissions, Atmos. Meas. Tech., 8, 3047–3057, https://doi.org/10.5194/amt-8-3047-2015, 2015.

Frey, M., Sha, M. K., Hase, F., Kiel, M., Blumenstock, T., Harig, R., Surawicz, G., Deutscher, N. M., Shiomi, K., Franklin, J. E., Bösch, H.,
445 Chen, J., Grutter, M., Ohyama, H., Sun, Y., Butz, A., Mengistu Tsidu, G., Ene, D., Wunch, D., Cao, Z., Garcia, O., Ramonet, M., Vogel, F., and Orphal, J.: Building the COllaborative Carbon Column Observing Network (COCCON): Long-Term Stability and Ensemble

Performance of the EM27/SUN Fourier Transform Spectrometer, Atmos. Meas. Tech., 12, 1513–1530, https://doi.org/10.5194/amt-12-1513-2019, 2019.

Fu, D., Pongetti, T. J., Blavier, J. F., Crawford, T. J., Manatt, K. S., Toon, G. C., Wong, K. W., and Sander, S. P.: Near-Infrared Remote
450   Sensing of Los Angeles Trace Gas Distributions from a Mountaintop Site, Atmos. Meas. Tech., 7, 713–729, https://doi.org/10.5194/amt-7-713-2014, 2014.

Gisi, M., Hase, F., Dohe, S., Blumenstock, T., Simon, A., and Keens, A.: XCO2-measurements with a Tabletop FTS Using Solar Absorption Spectroscopy, Atmos. Meas. Tech., 5, 2969–2980, https://doi.org/10.5194/amt-5-2969-2012, 2012.

Gordon, I. E., Rothman, L. S., Hargreaves, R. J., Hashemi, R., Karlovets, E. V., Skinner, F. M., Conway, E. K., Hill, C., Kochanov, R. V.,
455   Tan, Y., Wcisło, P., Finenko, A. A., Nelson, K., Bernath, P. F., Birk, M., Boudon, V., Campargue, A., Chance, K. V., Coustenis, A., Drouin,
B. J., Flaud, J. –., Gamache, R. R., Hodges, J. T., Jacquemart, D., Mlawer, E. J., Nikitin, A. V., Perevalov, V. I., Rotger, M., Tennyson,
J., Toon, G. C., Tran, H., Tyuterev, V. G., Adkins, E. M., Baker, A., Barbe, A., Canè, E., Császár, A. G., Dudaryonok, A., Egorov, O.,
Fleisher, A. J., Fleurbaey, H., Foltynowicz, A., Furtenbacher, T., Harrison, J. J., Hartmann, J. –., Horneman, V. –., Huang, X., Karman,
T., Karns, J., Kassi, S., Kleiner, I., Kofman, V., Kwabia–Tchana, F., Lavrentieva, N. N., Lee, T. J., Long, D. A., Lukashevskaya, A. A.,
460   Lyulin, O. M., Makhnev, V. Yu., Matt, W., Massie, S. T., Melosso, M., Mikhailenko, S. N., Mondelain, D., Müller, H. S. P., Naumenko,
O. V., Perrin, A., Polyansky, O. L., Raddaoui, E., Raston, P. L., Reed, Z. D., Rey, M., Richard, C., Tóbiás, R., Sadiek, I., Schwenke, D. W.,
Starikova, E., Sung, K., Tamassia, F., Tashkun, S. A., Vander Auwera, J., Vasilenko, I. A., Vigasin, A. A., Villanueva, G. L., Vispoel, B.,
Wagner, G., Yachmenev, A., and Yurchenko, S. N.: The HITRAN2020 Molecular Spectroscopic Database, J. Quant. Spectrosc. Ra., 277,
107 949, https://doi.org/10.1016/j.jqsrt.2021.107949, 2022.

465   Griffith, D. W. T., Pöhler, D., Schmitt, S., Hammer, S., Vardag, S. N., and Platt, U.: Long Open-Path Measurements of Greenhouse Gases in
Air Using near-Infrared Fourier Transform Spectroscopy, Atmos. Meas. Tech., 11, 1549–1563, https://doi.org/10.5194/amt-11-1549-2018,
2018.

Gurney, K. R., Patarasuk, R., Liang, J., Song, Y., O'Keeffe, D., Rao, P., Whetstone, J. R., Duren, R. M., Eldering, A., and Miller, C.:
The Hestia Fossil Fuel CO_2 Emissions Data Product for the Los Angeles Megacity (Hestia-LA), Earth. Syst. Sci. Data, 11, 1309–1335,
470   https://doi.org/10.5194/essd-11-1309-2019, 2019.

Gurney, K. R., Liang, J., Roest, G., Song, Y., Mueller, K., and Lauvaux, T.: Under-Reporting of Greenhouse Gas Emissions in U.S. Cities,
Nat. Commun., 12, 553, https://doi.org/10.1038/s41467-020-20871-0, 2021.

Hase, F., Blumenstock, T., and Paton-Walsh, C.: Analysis of the Instrumental Line Shape of High-Resolution Fourier Transform IR Spectrometers with Gas Cell Measurements and New Retrieval Software, Appl. Optics, 38, 3417–22, https://doi.org/10.1364/AO.38.003417,
475   1999.

Hase, F., Frey, M., Blumenstock, T., Groß, J., Kiel, M., Kohlhepp, R., Mengistu Tsidu, G., Schäfer, K., Sha, M. K., and Orphal, J.: Application
of Portable FTIR Spectrometers for Detecting Greenhouse Gas Emissions of the Major City Berlin, Atmos. Meas. Tech., 8, 3059–3068,
https://doi.org/10.5194/amt-8-3059-2015, 2015.

He, L., Zeng, Z.-C., Pongetti, T. J., Wong, C., Liang, J., Gurney, K. R., Newman, S., Yadav, V., Verhulst, K., Miller, C. E., Duren,
480   R., Frankenberg, C., Wennberg, P. O., Shia, R.-L., Yung, Y. L., and Sander, S. P.: Atmospheric Methane Emissions Correlate
With Natural Gas Consumption From Residential and Commercial Sectors in Los Angeles, Geophys. Res. Lett., 46, 8563–8571,
https://doi.org/10.1029/2019GL083400, 2019.

Hsu, A., Höhne, N., Kuramochi, T., Roelfsema, M., Weinfurter, A., Xie, Y., Lütkehermöller, K., Chan, S., Corfee-Morlot, J., Drost, P.,
Faria, P., Gardiner, A., Gordon, D. J., Hale, T., Hultman, N. E., Moorhead, J., Reuvers, S., Setzer, J., Singh, N., Weber, C., and Wider-

485   berg, O.: A Research Roadmap for Quantifying Non-State and Subnational Climate Mitigation Action, Nature Clim. Change., 9, 11–17, https://doi.org/10.1038/s41558-018-0338-z, 2019.

Huo, D., Huang, X., Dou, X., Ciais, P., Li, Y., Deng, Z., Wang, Y., Cui, D., Benkhelifa, F., Sun, T., Zhu, B., Roest, G., Gurney, K. R., Ke, P., Guo, R., Lu, C., Lin, X., Lovell, A., Appleby, K., DeCola, P. L., Davis, S. J., and Liu, Z.: Carbon Monitor Cities Near-Real-Time Daily Estimates of CO2 Emissions from 1500 Cities Worldwide, Sci. Data, 9, 533, https://doi.org/10.1038/s41597-022-01657-z, 2022.

490   Jacobson, A. R., Schuldt, K. N., Miller, J. B., Oda, T., Tans, P., Arlyn Andrews, Mund, J., Ott, L., Collatz, G. J., Aalto, T., Afshar, S., Aikin, K., Aoki, S., Apadula, F., Baier, B., Bergamaschi, P., Beyersdorf, A., Biraud, S. C., Bollenbacher, A., Bowling, D., Brailsford, G., Abshire, J. B., Chen, G., Huilin Chen, Lukasz Chmura, Sites Climadat, Colomb, A., Conil, S., Cox, A., Cristofanelli, P., Cuevas, E., Curcoll, R., Sloop, C. D., Davis, K., Wekker, S. D., Delmotte, M., DiGangi, J. P., Dlugokencky, E., Ehleringer, J., Elkins, J. W., Emmenegger, L., Fischer, M. L., Forster, G., Frumau, A., Galkowski, M., Gatti, L. V., Gloor, E., Griffis, T., Hammer, S., Haszpra, L.,

495   Hatakka, J., Heliasz, M., Hensen, A., Hermanssen, O., Hintsa, E., Holst, J., Jaffe, D., Karion, A., Kawa, S. R., Keeling, R., Keronen, P., Kolari, P., Kominkova, K., Kort, E., Krummel, P., Kubistin, D., Labuschagne, C., Langenfelds, R., Laurent, O., Laurila, T., Lauvaux, T., Law, B., Lee, J., Lehner, I., Leuenberger, M., Levin, I., Levula, J., Lin, J., Lindauer, M., Loh, Z., Lopez, M., Luijkx, I. T., Myhre, C. L., Machida, T., Mammarella, I., Manca, G., Manning, A., Manning, A., Marek, M. V., Marklund, P., Martin, M. Y., Matsueda, H., McKain, K., Meijer, H., Meinhardt, F., Miles, N., Miller, C. E., Mölder, M., Montzka, S., Moore, F., Josep-Anton Morgui, Morimoto,

500   S., Munger, B., Jaroslaw Necki, Newman, S., Nichol, S., Niwa, Y., O'Doherty, S., Mikaell Ottosson-Löfvenius, Paplawsky, B., Peischl, J., Peltola, O., Jean-Marc Pichon, Piper, S., Plass-Dölmer, C., Ramonet, M., Reyes-Sanchez, E., Richardson, S., Riris, H., Ryerson, T., Saito, K., Sargent, M., Sasakawa, M., Sawa, Y., Say, D., Scheeren, B., Schmidt, M., Schmidt, A., Schumacher, M., Shepson, P., Shook, M., Stanley, K., Steinbacher, M., Stephens, B., Sweeney, C., Thoning, K., Torn, M., Turnbull, J., Tørseth, K., Bulk, P. V. D., Dinther, D. V., Vermeulen, A., Viner, B., Vitkova, G., Walker, S., Weyrauch, D., Wofsy, S., Worthy, D., Dickon Young, and Miroslaw Zimnoch:

505   CarbonTracker CT2019B, https://doi.org/10.25925/20201008, 2020.

Kiel, M., Eldering, A., Roten, D. D., Lin, J. C., Feng, S., Lei, R., Lauvaux, T., Oda, T., Roehl, C. M., Blavier, J.-F., and Iraci, L. T.: Urban-Focused Satellite CO2 Observations from the Orbiting Carbon Observatory-3: A First Look at the Los Angeles Megacity, Remote Sens. Environ., 258, 112 314, https://doi.org/10.1016/j.rse.2021.112314, 2021.

Klappenbach, F., Bertleff, M., Kostinek, J., Hase, F., Blumenstock, T., Agusti-Panareda, A., Razinger, M., and Butz, A.: Accurate Mo-

510   bile Remote Sensing of XCO_2 and XCH_4 Latitudinal Transects from Aboard a Research Vessel, Atmos. Meas. Tech., 8, 5023–5038, https://doi.org/10.5194/amt-8-5023-2015, 2015.

Luther, A., Kleinschek, R., Scheidweiler, L., Defratyka, S., Stanisavljevic, M., Forstmaier, A., Dandocsi, A., Wolff, S., Dubravica, D., Wildmann, N., Kostinek, J., Jöckel, P., Nickl, A.-L., Klausner, T., Hase, F., Frey, M., Chen, J., Dietrich, F., Nęcki, J., Swolkień, J., Fix, A., Roiger, A., and Butz, A.: Quantifying CH_4 Emissions from Hard Coal Mines Using Mobile Sun-Viewing Fourier Transform Spectrometry,

515   Atmos. Meas. Tech., 12, 5217–5230, https://doi.org/10.5194/amt-12-5217-2019, 2019.

Luther, A., Kostinek, J., Kleinschek, R., Defratyka, S., Stanisavljević, M., Forstmaier, A., Dandocsi, A., Scheidweiler, L., Dubravica, D., Wildmann, N., Hase, F., Frey, M. M., Chen, J., Dietrich, F., Nęcki, J., Swolkień, J., Knote, C., Vardag, S. N., Roiger, A., and Butz, A.: Observational Constraints on Methane Emissions from Polish Coal Mines Using a Ground-Based Remote Sensing Network, Atmos. Chem. Phys., 22, 5859–5876, https://doi.org/10.5194/acp-22-5859-2022, 2022.

520   Maasakkers, J. D., Varon, D. J., Elfarsdóttir, A., McKeever, J., Jervis, D., Mahapatra, G., Pandey, S., Lorente, A., Borsdorff, T., Foorthuis, L. R., Schuit, B. J., Tol, P., van Kempen, T. A., van Hees, R., and Aben, I.: Using Satellites to Uncover Large Methane Emissions from Landfills, Science Advances, 8, eabn9683, https://doi.org/10.1126/sciadv.abn9683, 2022.

McKain, K., Down, A., Raciti, S. M., Budney, J., Hutyra, L. R., Floerchinger, C., Herndon, S. C., Nehrkorn, T., Zahniser, M. S., Jackson, R. B., Phillips, N., and Wofsy, S. C.: Methane Emissions from Natural Gas Infrastructure and Use in the Urban Region of Boston, Massachusetts, Proc. Natl. Acad. Sci. USA, 112, 1941–1946, https://doi.org/10.1073/pnas.1416261112, 2015.

Meirink, J. F., Eskes, H. J., and Goede, A. P. H.: Sensitivity Analysis of Methane Emissions Derived from SCIAMACHY Observations through Inverse Modelling, Atmos. Chem. Phys., 6, 1275–1292, https://doi.org/10.5194/acp-6-1275-2006, 2006.

Mitchell, L. E., Lin, J. C., Hutyra, L. R., Bowling, D. R., Cohen, R. C., Davis, K. J., DiGangi, E., Duren, R. M., Ehleringer, J. R., Fain, C., Falk, M., Guha, A., Karion, A., Keeling, R. F., Kim, J., Miles, N. L., Miller, C. E., Newman, S., Pataki, D. E., Prinzivalli, S., Ren, X., Rice, A., Richardson, S. J., Sargent, M., Stephens, B. B., Turnbull, J. C., Verhulst, K. R., Vogel, F., Weiss, R. F., Whetstone, J., and Wofsy, S. C.: A Multi-City Urban Atmospheric Greenhouse Gas Measurement Data Synthesis, Sci. Data, 9, 361, https://doi.org/10.1038/s41597-022-01467-3, 2022.

Mueller, K. L., Lauvaux, T., Gurney, K. R., Roest, G., Ghosh, S., Gourdji, S. M., Karion, A., DeCola, P., and Whetstone, J.: An Emerging GHG Estimation Approach Can Help Cities Achieve Their Climate and Sustainability Goals, Environ. Res. Lett., 16, 084 003, https://doi.org/10.1088/1748-9326/ac0f25, 2021.

National Centers for Environmental Prediction, National Weather Service, NOAA, U.S. Department of Commerce: NCEP FNL Operational Model Global Tropospheric Analyses, Continuing from July 1999, https://doi.org/10.5065/D6M043C6, 2000.

Pitt, J. R., Lopez-Coto, I., Hajny, K. D., Tomlin, J., Kaeser, R., Jayarathne, T., Stirm, B. H., Floerchinger, C. R., Loughner, C. P., Gately, C. K., Hutyra, L. R., Gurney, K. R., Roest, G. S., Liang, J., Gourdji, S., Karion, A., Whetstone, J. R., and Shepson, P. B.: New York City Greenhouse Gas Emissions Estimated with Inverse Modeling of Aircraft Measurements, Elem. Sci. Anth., 10, 00 082, https://doi.org/10.1525/elementa.2021.00082, 2022.

Queißer, M., Granieri, D., and Burton, M.: A New Frontier in CO_2 Flux Measurements Using a Highly Portable DIAL Laser System, Sci. Rep., 6, 33 834, https://doi.org/10.1038/srep33834, 2016.

Reuter, M., Buchwitz, M., Schneising, O., Krautwurst, S., O'Dell, C. W., Richter, A., Bovensmann, H., and Burrows, J. P.: Towards Monitoring Localized CO_2 Emissions from Space: Co-Located Regional CO_2 and NO_2 Enhancements Observed by the OCO-2 and S5P Satellites, Atmos. Chem. Phys., 19, 9371–9383, https://doi.org/10.5194/acp-19-9371-2019, 2019.

Rieker, G. B., Giorgetta, F. R., Swann, W. C., Kofler, J., Zolot, A. M., Sinclair, L. C., Baumann, E., Cromer, C., Petron, G., Sweeney, C., Tans, P. P., Coddington, I., and Newbury, N. R.: Frequency-Comb-Based Remote Sensing of Greenhouse Gases over Kilometer Air Paths, Optica, 1, 290–298, https://doi.org/10.1364/OPTICA.1.000290, 2014.

Sargent, M. R., Floerchinger, C., McKain, K., Budney, J., Gottlieb, E. W., Hutyra, L. R., Rudek, J., and Wofsy, S. C.: Majority of US Urban Natural Gas Emissions Unaccounted for in Inventories, Proc. Natl. Acad. Sci. USA, 118, e2105804 118, https://doi.org/10.1073/pnas.2105804118, 2021.

Toon, G. C.: Solar Line List for the TCCON 2014 Data Release, https://doi.org/10.14291/TCCON.GGG2014.SOLAR.R0/1221658, 2015.

Turnbull, J. C., Karion, A., Davis, K. J., Lauvaux, T., Miles, N. L., Richardson, S. J., Sweeney, C., McKain, K., Lehman, S. J., Gurney, K. R., Patarasuk, R., Liang, J., Shepson, P. B., Heimburger, A., Harvey, R., and Whetstone, J.: Synthesis of Urban CO_2 Emission Estimates from Multiple Methods from the Indianapolis Flux Project (INFLUX), Environ. Sci. Technol., 53, 287–295, https://doi.org/10.1021/acs.est.8b05552, 2019.

Turner, A. J., Kim, J., Fitzmaurice, H., Newman, C., Worthington, K., Chan, K., Wooldridge, P. J., Köehler, P., Frankenberg, C., and Cohen, R. C.: Observed Impacts of COVID-19 on Urban CO_2 Emissions, Geophys. Res. Lett., 47, e2020GL090 037, https://doi.org/10.1029/2020GL090037, 2020.

Verhulst, K. R., Karion, A., Kim, J., Salameh, P. K., Keeling, R. F., Newman, S., Miller, J., Sloop, C., Pongetti, T., Rao, P., Wong, C., Hopkins, F. M., Yadav, V., Weiss, R. F., Duren, R. M., and Miller, C. E.: Carbon Dioxide and Methane Measurements from the Los Angeles Megacity Carbon Project – Part 1: Calibration, Urban Enhancements, and Uncertainty Estimates, Atmos. Chem. Phys., 17, 8313–8341, https://doi.org/10.5194/acp-17-8313-2017, 2017.

565 Wei, T., Wu, J., and Chen, S.: Keeping Track of Greenhouse Gas Emission Reduction Progress and Targets in 167 Cities Worldwide, Front. Sustain. Cities, 3, https://doi.org/10.3389/frsc.2021.696381, 2021.

Wennberg, P. O., Roehl, C., Wunch, D., Blavier, J.-F., Toon, G. C., Allen, N. T., Treffers, R., and Laughner, J.: TCCON Data from Caltech (US), Release GGG2020.R0, https://doi.org/10.14291/tccon.ggg2020.pasadena01.R0, 2022.

Wong, C. K., Pongetti, T. J., Oda, T., Rao, P., Gurney, K. R., Newman, S., Duren, R. M., Miller, C. E., Yung, Y. L., and Sander, S. P.:
570 Monthly Trends of Methane Emissions in Los Angeles from 2011 to 2015 Inferred by CLARS-FTS Observations, Atmos. Chem. Phys., 16, 13 121–13 130, https://doi.org/10.5194/acp-16-13121-2016, 2016.

Wong, K. W., Fu, D., Pongetti, T. J., Newman, S., Kort, E. A., Duren, R., Hsu, Y. K., Miller, C. E., Yung, Y. L., and Sander, S. P.: Mapping CH4 : CO2 Ratios in Los Angeles with CLARS-FTS from Mount Wilson, California, Atmos. Chem. Phys., 15, 241–252, https://doi.org/10.5194/acp-15-241-2015, 2015.

575 Wunch, D., Toon, G. C., Blavier, J.-F. L., Washenfelder, R. A., Notholt, J., Connor, B. J., Griffith, D. W. T., Sherlock, V., and Wennberg, P. O.: The Total Carbon Column Observing Network, Philos. T. R. Soc. A, 369, 2087–2112, https://doi.org/10.1098/rsta.2010.0240, 2011.

Ye, X., Lauvaux, T., Kort, E. A., Oda, T., Feng, S., Lin, J. C., Yang, E. G., and Wu, D.: Constraining Fossil Fuel CO2 Emissions From Urban Area Using OCO-2 Observations of Total Column CO2, J. Geophys. Res. Atmos., 125, e2019JD030 528, https://doi.org/10.1029/2019JD030528, 2020.

580 Zeng, Z.-C., Zhang, Q., Natraj, V., Margolis, J. S., Shia, R.-L., Newman, S., Fu, D., Pongetti, T. J., Wong, K. W., Sander, S. P., Wennberg, P. O., and Yung, Y. L.: Aerosol Scattering Effects on Water Vapor Retrievals over the Los Angeles Basin, Atmos. Chem. Phys., 17, 2495–2508, https://doi.org/10.5194/acp-17-2495-2017, 2017.

Zeng, Z.-C., Wang, Y., Pongetti, T. J., Gong, F.-Y., Newman, S., Li, Y., Natraj, V., Shia, R.-L., Yung, Y. L., and Sander, S. P.: Tracking the Atmospheric Pulse of a North American Megacity from a Mountaintop Remote Sensing Observatory, Remote Sens. Environ., 248,
585 112 000, https://doi.org/10.1016/j.rse.2020.112000, 2020a.

Zeng, Z.-C., Xu, F., Natraj, V., Pongetti, T. J., Shia, R.-L., Zhang, Q., Sander, S. P., and Yung, Y. L.: Remote Sensing of Angular Scattering Effect of Aerosols in a North American Megacity, Remote Sens. Environ., 242, 111 760, https://doi.org/10.1016/j.rse.2020.111760, 2020b.

Zeng, Z.-C., Natraj, V., Xu, F., Chen, S., Gong, F.-Y., Pongetti, T., Sung, K., Toon, G., Sander, S., and Yung, Y.: GFIT3: A Full Physics Retrieval Algorithm for Remote Sensing of Greenhouse Gases in the Presence of Aerosols, Atmos. Meas. Tech., 14, 6483–6507,
590 https://doi.org/10.5194/amt-14-6483-2021, 2021.

Zeng, Z.-C., Pongetti, T., Newman, S., Oda, T., Gurney, K., Palmer, P. I., Yung, Y. L., and Sander, S. P.: Decadal Decrease in Los Angeles Methane Emissions Is Much Smaller than Bottom-up Estimates, Nat. Commun., 14, 5353, https://doi.org/10.1038/s41467-023-40964-w, 2023.

Zhang, Q., Natraj, V., Li, K.-F., Shia, R.-L., Fu, D., Pongetti, T. J., Sander, S. P., Roehl, C. M., and Yung, Y. L.: Accounting for
595 Aerosol Scattering in the CLARS Retrieval of Column Averaged CO2 Mixing Ratios, J. Geophys. Res. Atmos., 120, 7205–7218, https://doi.org/10.1002/2015JD023499, 2015.